Check for updates

ADVANCING EARTH AND SPACE SCIENCES

JGR Biogeosciences

RESEARCH ARTICLE
10.1029/2025JG009240

Tracking Water Dynamics of a Temperate Forest Under Drought and Non-Drought Conditions Using Active and Passive Microwave and Optical Remote Sensing

Florian M. Hellwig[1,2,3], Anke Fluhrer[1], Clémence Dubois[3,4], Konstantin Schellenberg[3,5], David Chaparro[1,6], Markus Zehner[3], Anne Klosterhalfen[7], María Piles[8], Christiane Schmullius[3], Harald Kunstmann[2,9,10], and Thomas Jagdhuber[1,2]

[1]German Aerospace Center (DLR), Microwaves and Radar Institute, Wessling, Germany, [2]University of Augsburg, Institute of Geography, Augsburg, Germany, [3]Department for Earth Observation, Friedrich Schiller University Jena, Jena, Germany, [4]German Aerospace Center (DLR), Institute of Data Science, Jena, Germany, [5]Department of Biogeochemical Processes, Max-Planck Institute for Biogeochemistry, Jena, Germany, [6]Centre for Ecological and Forestry Applications (CREAF), Cerdanyola del Vallès, Spain, [7]University of Göttingen, Bioclimatology, Göttingen, Germany, [8]University of Valencia, Image Processing Laboratory, Valencia, Spain, [9]Institute of Meteorology and Climate Research, Karlsruhe Institute of Technology, Karlsruhe, Germany, [10]Center for Climate Resilience, University of Augsburg, Augsburg, Germany

Key Points:

- Sentinel-1 VH is sensitive to Leaf Area Index under wet and leaf-on conditions, and to topsoil moisture under dry and leaf-off conditions
- X- and C-band Relative Water Content can capture a drought onset through fast water content changes in leaves and twigs of the top canopy
- L-band Relative Water Content can capture drought legacy effects via slow water content changes in branches and trunks of the lower canopy

Supporting Information:

Supporting Information may be found in the online version of this article.

Correspondence to:

F. M. Hellwig,
florian.hellwig@dlr.de

Citation:

Hellwig, F. M., Fluhrer, A., Dubois, C., Schellenberg, K., Chaparro, D., Zehner, M., et al. (2026). Tracking water dynamics of a temperate forest under drought and non-drought conditions using active and passive microwave and optical remote sensing. *Journal of Geophysical Research: Biogeosciences*, *131*, e2025JG009240. https://doi.org/10.1029/2025JG009240

Received 8 JUL 2025
Accepted 17 APR 2026

Author Contributions:

Conceptualization: Florian M. Hellwig, Anke Fluhrer, Clémence Dubois, Thomas Jagdhuber
Data curation: Florian M. Hellwig, Anke Fluhrer, Markus Zehner, Anne Klosterhalfen
Formal analysis: Florian M. Hellwig
Funding acquisition: Florian M. Hellwig, Anke Fluhrer, David Chaparro, Harald Kunstmann, Thomas Jagdhuber
Investigation: Florian M. Hellwig, Anke Fluhrer, Clémence Dubois, Konstantin Schellenberg, David Chaparro, Markus Zehner, Anne Klosterhalfen, María Piles, Thomas Jagdhuber

Abstract Water status, water dynamics, and ecohydrological resilience of a protected German beech forest during the 2018–2020 multi-year drought are assessed using over six years of multi-frequency remote sensing data, integrating active, passive, and optical sensors with varying canopy penetration depths, highlighting the importance of monitoring forests under extreme conditions. In this study, we investigate Sentinel-1 C-band backscatter (S-1 γ^0) and the relative water content estimated from vegetation optical depth (RWC_{VOD}) of AMSR2 (X- and C-bands) and SMAP (L-band) within the soil-plant-atmosphere system (SPAS). In addition, time series are intercompared and examined through correlation and sensitivity analyses applying tailored environmental and newly developed hydrological selection strategies. Our results show that S-1 γ_{VH} is most influenced by leaf area index and thus leaf biomass when sensed during dense vegetation (leaf-on), no-frost, and very wet conditions ($r = -0.94$). In contrast, during sparse vegetation (leaf-off), no-frost, stable dry-down, and extremely dry conditions, S-1 γ_{VH} is very sensitive to topsoil moisture ($r = 0.91$). Due to increased microwave attenuation, resulting in reduced S-1 γ_{VH} backscatter, an anti-cyclical behavior (negative correlations) is observed between almost all SPAS-based variables/proxies and S-1 γ_{VH} during leaf-on conditions. Conversely, this reverses to a cyclical behavior (positive correlations) during leaf-off conditions. Our results reveal that X- and C-band RWC_{VOD} effectively detect drought onset by capturing fast water content changes in leaves and twigs of the top canopy due to shallow sensing depth, while L-band RWC_{VOD} captures legacy effects after repetitive droughts through slower water content changes in branches and trunks of lower tree compartments.

Plain Language Summary Continuous forest monitoring is becoming increasingly important due to climate change and extreme events. The 2018–2020 multi-year drought caused severe damage to forests in Central Europe. Using satellite remote sensing data, we analyze the water status and water dynamics of a protected German beech forest during this drought. Sensors onboard active microwave satellites transmit longwave electromagnetic radiation toward the Earth's surface, which can penetrate clouds and operate during daytime and nighttime. These microwaves interact with objects on the Earth's surface and are scattered back to the satellite sensor. Passive microwave sensors do not actively send electromagnetic radiation, but passively measure the natural emission. Our results show that active microwave data are most influenced by leaf biomass when sensed during dense vegetation (leaf-on) and very wet conditions. In contrast, these data are very sensitive to topsoil moisture during sparse vegetation (leaf-off) and extremely dry conditions. Our results reveal that passive microwave data of shorter wavelengths can detect drought onset by capturing fast water content changes in leaves and twigs of the top canopy. Conversely, data of longer wavelengths capture legacy effects from past drought conditions through slower water content changes in branches and trunks of lower tree compartments.

1. Introduction

Water in forests supports essential ecosystem processes, including carbon sequestration, hydrologic regulation, and biodiversity preservation (McDowell et al., 2022). However, human-induced climate change is leading to

Methodology: Florian M. Hellwig, Anke Fluhrer, Clémence Dubois, Konstantin Schellenberg, David Chaparro, Thomas Jagdhuber
Project administration: Christiane Schmullius, Harald Kunstmann, Thomas Jagdhuber
Resources: Clémence Dubois, Markus Zehner, Anne Klosterhalfen, Christiane Schmullius, Harald Kunstmann, Thomas Jagdhuber
Software: Florian M. Hellwig, Anke Fluhrer, Markus Zehner
Supervision: Anke Fluhrer, Clémence Dubois, Christiane Schmullius, Harald Kunstmann, Thomas Jagdhuber
Validation: Florian M. Hellwig
Visualization: Florian M. Hellwig
Writing – original draft: Florian M. Hellwig, Anke Fluhrer, Clémence Dubois, Thomas Jagdhuber
Writing – review & editing: Florian M. Hellwig, Anke Fluhrer, Clémence Dubois, Konstantin Schellenberg, David Chaparro, Markus Zehner, Anne Klosterhalfen, María Piles, Christiane Schmullius, Harald Kunstmann, Thomas Jagdhuber

increasing temperatures, which in turn increases the frequency and severity of droughts. Furthermore, the lack of precipitation reduces water storage within trees, contributing to widespread forest mortality and increased flammability, which puts ecosystems at risk (Lee et al., 2023). Therefore, monitoring forest water status is vital for assessing forest health. In addition, studying how forest water dynamics interact with soil, plant, and atmospheric conditions is essential to understanding the role of plants within the soil-plant-atmosphere system (SPAS) (Beer et al., 2010; Gentine et al., 2019; Novick et al., 2022). The SPAS is understood as a holistic system that describes the simultaneous and interdependent exchange of mass (water), momentum (wind), and energy (temperature) between the soil, plant, and atmosphere components (Gardner, 1960, 1965; Nobel, 2020).

To track the forest water status and dynamics under drought conditions, SPAS-based variables can be divided into water storage (e.g., the vegetation water content, VWC, or the relative water content, RWC; Konings et al., 2021; Martínez-Vilalta et al., 2019; Rao et al., 2019), water potential (Ψ, which refers to the potential energy of water; Reichardt & Timm, 2020), and water fluxes (such as evapotranspiration, ET (Bastos et al., 2020; Giardina et al., 2023), sap flux (Poyatos et al., 2021) or plant water uptake, PWU; Feldman et al., 2023). When the water storage declines, the water potential becomes more negative, increasing the tension in the xylem, the network of vessels that drives the water flux from the roots to the leaves. This increased xylem tension can eventually lead to water flow disruption within trees by cavitation. Cavitation impairs forest health and can lead to tree mortality (Lambers & Oliveira, 2019). The severity of droughts increases these effects, with impacts on forest ecosystems varying widely from mild, asymptomatic water stress to significant tree mortality episodes, depending on the intensity and duration of the drought (Hammond et al., 2022).

The vitality and health of forests can be evaluated through forest inventories or field studies, such as the annually conducted Forest Condition Survey for Germany (TMIL, 2022). Additionally, continuous in situ data collection at specific sites enables long-term forest ecosystem monitoring. Networks of standardized monitoring stations, such as the Integrated Carbon Observation System (ICOS), are especially well-suited for this purpose. ICOS mainly monitors key greenhouse gases at roughly 170 stations in 16 European countries, next to environmental variables, mostly using the eddy-covariance technique (ICOS RI, 2024). However, forest inventories are conducted at relatively long intervals (e.g., decadal), and in situ measurements are spatially limited and sparse. Remote sensing provides a more effective alternative for regularly monitoring forest conditions; it is less time-consuming and provides a higher spatio-temporal coverage (Lausch et al., 2018). Space-borne sensors operating in the microwave domain can monitor forest water status with high temporal resolution over a large area independently of daylight and weather conditions (Ulaby et al., 1986). In contrast to optical remote sensing, which operates at nanometer to micrometer wavelengths, microwave remote sensing operates at longer wavelengths. This enables penetration into the canopy, receiving signals not only from the top of the trees (leaves and twigs) but also from the deeper layers (branches and trunks) and even from the soil, depending on the frequency (Chaparro et al., 2024; Konings et al., 2019). In addition, microwave remote sensing is more sensitive to vegetation's structural components and its dielectric properties (Ulaby et al., 1986), making it particularly suitable for monitoring water status and dynamics as well as the drought-induced water stress (e.g., Konings et al., 2019; Konings et al., 2021).

Sentinel-1 C-band synthetic aperture radar (SAR) data are often used to derive soil moisture (SM) on the continental to field scale when high spatial resolution is required. For instance, Bauer-Marschallinger et al. (2019), Foucras et al. (2020), and Gao et al. (2017) demonstrated that with a change detection algorithm, SM can be estimated under sparse vegetation (e.g., non-forested areas). Additionally, Sentinel-1 SAR data can also be used to enhance the spatial resolution of coarser passive microwave-based global SM products (Das et al., 2017). Vreugdenhil et al. (2018) showed the capability of Sentinel-1 data to monitor VWC over agricultural land using a random forest (RF) regression model. However, the proposed machine-learning approach lacks physical interpretability, and hence, its applicability across different ecological contexts is somewhat limited and has not yet been applied to forests (Vreugdenhil et al., 2018). The same applies to the RF model of M. M. El Hajj et al. (2023), from which the PWU for very dense olive orchards under dry conditions was estimated using Sentinel-1 data. Regarding evapotranspiration (ET), the sum of land surface evaporation and vegetation transpiration, Mueller et al. (2022) and Jagdhuber et al. (2023) observed a similar multiannual seasonally fluctuating behavior between Sentinel-1 SAR data and ET for coniferous forests.

Limitations of SAR for forestry studies include the lack of freely available L-band (i.e., low frequency) data, so that deep sensing depth into the canopy is currently lacking, and the fact that radar backscatter is not only sensitive to water but strongly influenced by vegetation structure (Konings et al., 2019; Ulaby et al., 1986). L-band from radiometers has been used to derive water-related SPAS-based variables at a coarse resolution (∼10–50 km) (Chaparro et al., 2021, 2024; Forkel et al., 2023; Konings et al., 2021; Steele-Dunne et al., 2017). The combination of active and passive microwave remote sensing, as demonstrated in the multi-frequency Soil Moisture Active Passive (SMAP)/Sentinel-1 SM product (Das et al., 2017), could help to overcome the limitations of active-only or passive-only techniques. The vegetation optical depth (VOD), mostly derived from passive microwave radiometers, describes the attenuation that the vegetation canopy exerts over land microwave emissions. Hence, VOD depends mainly on the water content of vegetation, its dry biomass, and structure, and is influenced by temperature and salinity (Chaparro et al., 2021; Jackson & Schmugge, 1991; Jagdhuber et al., 2022; Konings et al., 2019; Zhao et al., 2024). Previous studies have shown that VOD can be used to estimate water reservoirs and fluxes within the SPAS (see review by Konings et al. (2021)). Chaparro et al. (2024) used a multi-sensor approach consisting of LiDAR, microwave radiometers (Ku-, X-, and L-band), and SAR (C-band) to isolate the live fuel moisture content (LFMC) from the VOD signal. Rao et al. (2020) merged Landsat-8 surface reflectance and Sentinel-1 radar backscatter to obtain LFMC maps over the western United States. These studies demonstrate an essential complementarity among active and passive microwave and optical remote sensing.

Furthermore, Konings et al. (2019) provided information on how biomass and water storage can be estimated using microwaves. Forkel et al. (2023) demonstrated that LFMC could be globally estimated from the synergy of L-band VOD and leaf area index (LAI). The authors found more agreement for sparser vegetation than denser vegetation, such as needleleaf forests. In addition, Rao et al. (2019) demonstrated how X-band VOD can be directly converted into RWC by a location-dependent normalization of VOD. However, this RWC derivation is not independent of the dry biomass of vegetation due to phenological imprints (Martínez-Vilalta et al., 2019). Alternatively, Hellwig et al. (2023) selected a period with effectively constant biomass and plant structure conditions to estimate RWC from VOD under different hydrological conditions. In addition, Feldman et al. (2018) derived VWC from the L-band SMAP radiometer and analyzed the relationship between SM and PWU for dry-downs. Jagdhuber et al. (2025) went one step further and derived gravimetric vegetation water content (m_g) and RWC from ground-based L-band radiometry to ultimately estimate forest water potential. Beyond that, Jagdhuber et al. (2022) presented a novel study in the context of SPAS using a ground-based L-band radiometer, auxiliary information, and models to estimate water potential and water fluxes, such as PWU and ET, for a winter wheat field, based on the m_g estimation approach of Fink et al. (2018) and Meyer et al. (2019).

Overall, all these studies demonstrated that water-related SPAS-based proxies can be estimated from active and passive microwave and optical remote sensing. However, most studies are limited to only water storage estimations and either mask forests or assume stable hydrological conditions. In addition, except for Jagdhuber et al. (2022), these studies are mainly restricted to analyzing one or two SPAS-based variables. The relationship between microwave remote sensing and the entire SPAS, especially under different hydrological conditions in a forest ecosystem, remains poorly understood. In addition, a large information gap exists, as current assessments of forest water status rely on limited, single tree-scale measurements rarely compiled into regional or global databases (Novick et al., 2022).

Therefore, we use an unprecedented combination of more than 6 years of multi-frequency active and passive microwave and optical as well as in situ data to examine the water-related SPAS-based variables (e.g., SM) and SPAS-based proxies (e.g., LAI from remote sensing (RS)) and assess the water status and dynamics of a temperate forest under drought and non-drought conditions between October 2014 and December 2020. We selected a deciduous broadleaf forest in central Germany, as it was one of the highly impacted forests during the exceptional 2018–2020 multi-year drought in Central Europe. This multi-year drought has caused devastating damage, with severe leaf burns, premature leaf shedding, and even full canopy dieback being observed (Gharun et al., 2024; Philipp et al., 2021; Rakovec et al., 2022; Schuldt et al., 2020; Thonfeld et al., 2022; TMIL, 2022). In addition, we analyze time series of Sentinel-1 C-band backscatter as well as $\mathrm{RWC}_{\mathrm{VOD}}$ derived from Advanced Microwave Scanning Radiometer 2 (AMSR2) X- and C-band and SMAP L-band VOD (RS-based variables), and compare them to in situ SPAS-based variables and SPAS-based proxies using optical RS. The goal of this study is to understand how different SPAS-based variables and proxies (hereafter referred to as SPAS-based variables/proxies) are related to each other and to RS data, ultimately to understand and assess the water status and dynamics of a temperate forest under both drought and non-drought conditions. For this purpose, tailored

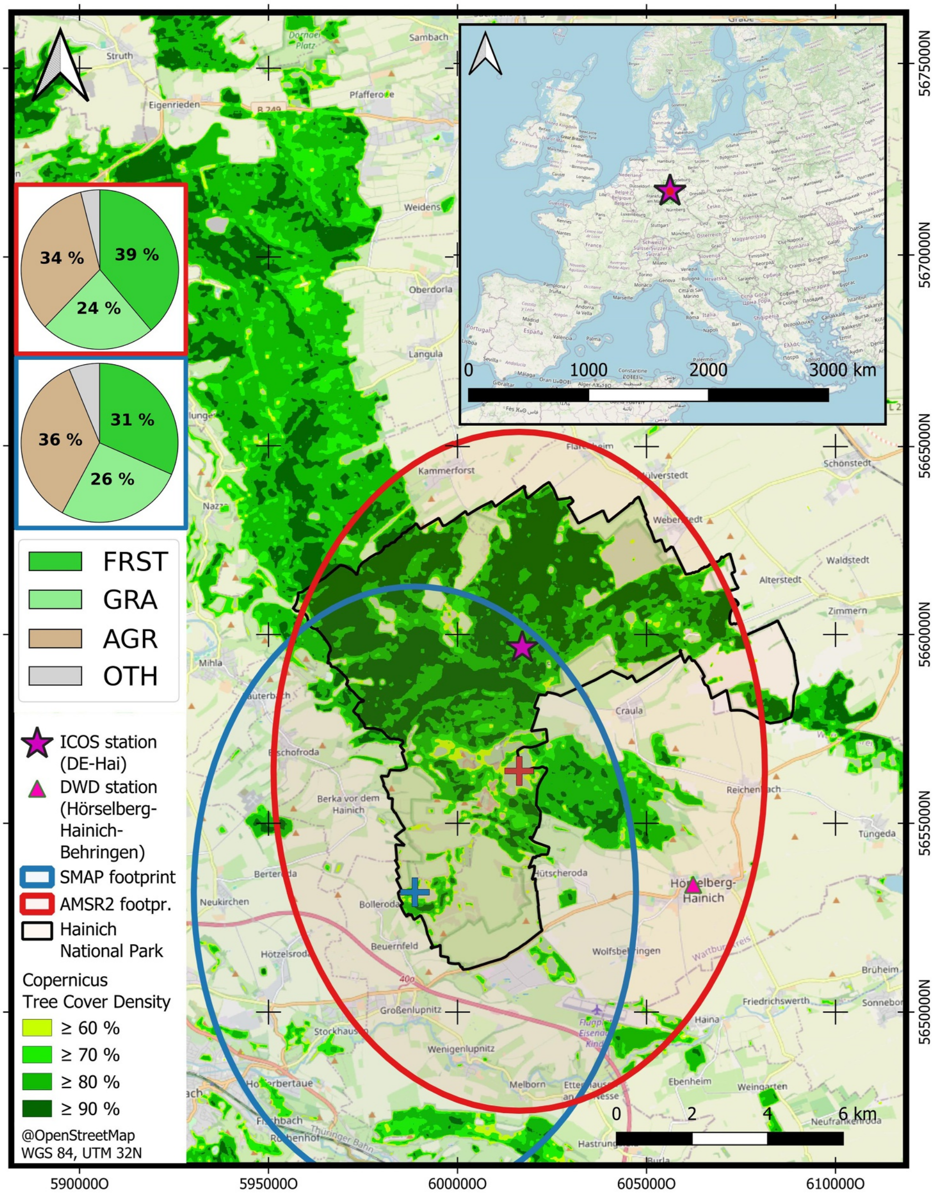

Figure 1. Location of the study site (Hainich Forest) in Germany, as well as in situ (DWD, 2021; Knohl et al., 2022), microwave remote sensing (footprint with center coordinates) (Jeu & Owe, 2014; Owe et al., 2008; Truckenbrodt, Freemantle, et al., 2019), Copernicus high resolution tree cover density (EAA, 2020), and CORINE land cover data (FRST = forest, GRA = grassland, AGR = agriculture, OTH = other) (EAA, 2019); pixel representation: due to the curvature of the earth, the pixels were shown as ellipses instead of squares, which is more realistic; footprint selection: due to the coarse spatial resolution of the passive microwave remote sensing data, only one pixel was selected from each data set whose center coordinates were within the Hainich National Park, that covers the ICOS station and has a high forest coverage. None of the other neighboring pixels fulfill these criteria.

environmental and new hydrological selection strategies are developed, and correlation, sensitivity, and time lag analyses are conducted.

2. Data

2.1. Study Site

This study was conducted in the Hainich Forest (including the National Park Hainich) located in the western part of the Free State of Thuringia in central Germany (51.08°N, 10.45°W) (Figure 1). Covering an area of around

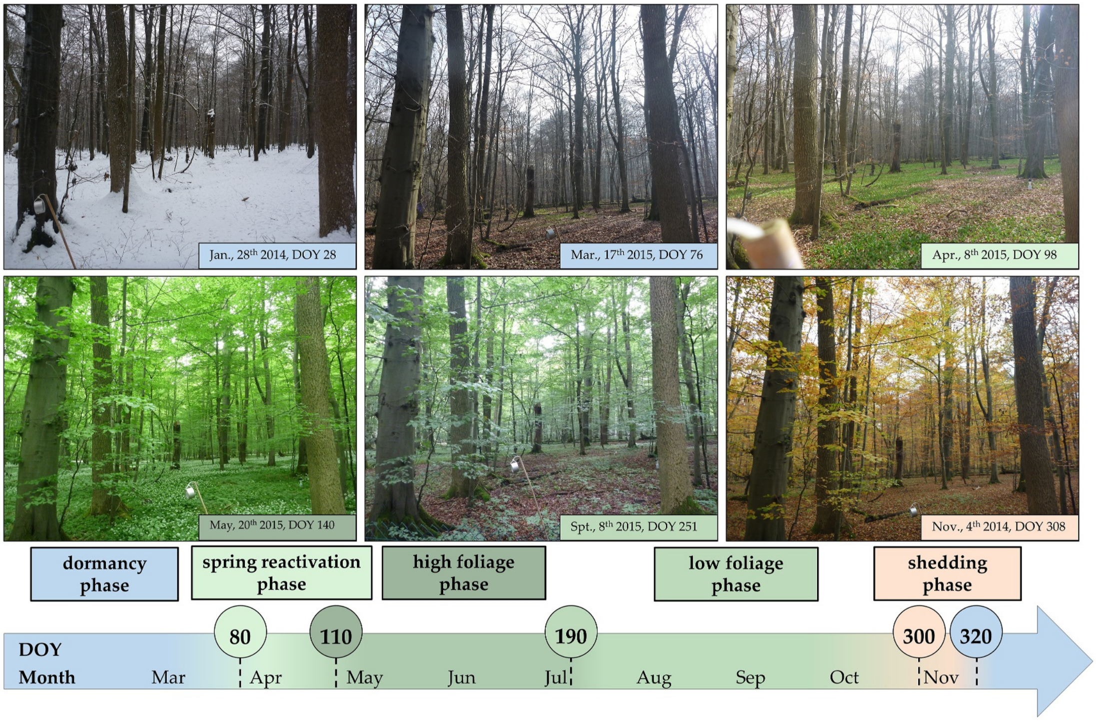

Figure 2. The five different vegetation phases in the Hainich Forest, classified based on biweekly in situ vegetation images taken from 2014 to 2016 by the Bioclimatology group of the University of Göttingen at the "DE-Hai" Integrated Carbon Observation System (ICOS) station: dormancy phase (day of the year (DOY): 321–79), spring reactivation phase (DOY: 80–109), high foliage phase (DOY: 110–189), low foliage phase (DOY: 190–299) and shedding phase (DOY: 300–320).

900 km^2, the study site shows a mean annual temperature of 8.6°C, with January being the coldest month (−0.4°C) and July being the warmest month (17.5°C), as well as the highest rainfall between May and August, compared to 2000–2020 (Knohl et al., 2022). The last few years have been considerably warmer than usual compared to the reference period (2000–2020), in particular, 2018 (+15% or +1.3°C), 2019 (+12% or +1.1°C), and 2020 (+14% or +1.2°C) (Knohl et al., 2022). In addition, a substantial deviation from the average rainfall (636 mm) is observed in these years, with 2018 being extremely dry (−28% or −176 mm) and 2017 very wet (+21% or +134 mm) compared to 2000–2020 (DWD, 2021). We used the study period from October 2014 to December 2020 because of the strong coincidence of droughts during these years.

The Hainich National Park is an unmanaged deciduous broadleaf forest on limestone, dominated by European beech (*Fagus sylvatica*, 65%), and with ash (*Fraxinus excelsior*, 25%) and maple (*Acer pseudoplatanus* and *platanoides*, 7%) mixing in the tree species composition substantially. The understory is dominated by spring bloomers, that is, geophytes, especially wild garlic (*Allium ursinum*) and wood anemone (*Anemone nemorosa*), which bloom between March/April and June/July, respectively. In contrast, the northern part of the Hainich Forest is managed, less dense, and younger (Figure 1) (Nationalpark-Verwaltung, 2023).

We subdivided each year into five different vegetation phases to better reflect the vegetation dynamics of the Hainich National Park, such as leaf-on and leaf-off conditions (Figure 2). While the vegetation is dormant during the winter (dormancy phase), the understory begins to grow in March (spring reactivation phase). The foliage of the beech trees starts in April/May (high foliage phase). In late summer, the understory fades, and the tree canopies become less dense (low foliage phase). Finally, the beeches shed their leaves in October/November (shedding phase), falling into winter dormancy.

Regarding the land cover in the study site (Figure 1), the study pixels of the passive microwave remote sensing data are partially covered by dense forests (∼30–40%), agriculture (∼35%), and grassland (∼25%). The dense tree cover of the Hainich National Park (southern Hainich Forest) indicates high forest biomass and, therefore, high vegetation water content. VOD is strongly sensitive to both, as it reflects the attenuation of microwaves through vegetation. Since forests have significantly larger biomass and water content than sparse vegetation, even

Table 1
Overview of All In Situ Data Sets Utilized in This Study (ICOS = Integrated Carbon Observation System, DWD = German Meteorological Service, SM = Soil Moisture, TS = Soil Temperature, TA = Air Temperature, LE = Latent Heat Flux, VPD = Vapor Pressure Deficit, RH = Relative Air Humidity)

Type of data set	Data set	Main variable(s)	Time period	Temporal resolution	Reference
In Situ	ICOS	SM, TS, TA, LE, RH, VPD	10/2014-12/2020	half-hourly, daily	Knohl et al. (2022)
	DWD	Precipitation	10/2014-12/2020	hourly	DWD (2021)
	Vegetation Images	–	01/2014-05/2023	irregular	–

moderate forest coverage is expected to have a substantial frequency-related impact on microwave attenuation and, consequently, VOD (Chaparro et al., 2021; Jackson & Schmugge, 1991; Jagdhuber et al., 2022; Konings et al., 2019). Therefore, the VOD signal should be dominated by the high forest biomass and water content in the Hainich National Park and within the study pixels, even for moderate forest coverage. In addition, the VOD patterns explained later remain very similar for adjacent pixels with higher forest coverage (not shown). These pixels lie outside the ICOS station and cover mainly the northern and managed part of the Hainich Forest, which has a lower tree height and tree cover density, and were therefore excluded.

2.2. In Situ Data

The in situ data were primarily obtained from the Integrated Carbon Observation System (ICOS) station "DE-Hai" located at the center of the study site (Figure 1, Table 1). This station provides standardized half-hourly in situ data accessible through the ICOS network (Knohl et al., 2022). For analyses conducted in this study, soil moisture (SM) at 8, 16, and 32 cm soil depth, soil temperature (TS) at 2 cm soil depth, air temperature (TA) at 2 m height, as well as latent heat flux (LE), relative air humidity (RH) and vapor pressure deficit (VPD) at 44 m height were selected. The 95th percentile of TA (TA_{95}) was also chosen for drought analyses because it better represents extreme heat conditions than the mean. Due to data gaps, hourly precipitation data from the nearest weather station from the German Meteorological Service (DWD) ("Hörselberg-Hainich-Behringen" (ID 00336), ~7.5 km) with the most similar data on an hourly basis ($r = 0.9$) was also utilized (DWD, 2021). Additionally, various vegetation images were included to characterize the vegetation dynamics.

2.3. Remote Sensing Data

Table 2 provides an overview of the different microwave and optical remote sensing data considered in this study.

The Copernicus Sentinel-1 mission represents a constellation of two polar-orbiting satellites and provides C-band synthetic aperture radar (SAR) data (5.405 GHz). It is operated by the European Space Agency (ESA). Data from both satellites (Sentinel-1A, -1B) were considered, acquired in the interferometric wide swath mode (IW) with 10 m pixel spacing (GRD) (Table 2), and preprocessed (Section 3.1) (Truckenbrodt, Cremer, et al., 2019).

In addition, two VOD data sets from passive microwave satellites were employed (Table 2). The first data set is based on the Global Change Observation Mission (GCOM) Advanced Microwave Scanning Radiometer 2 (AMSR2) X- (10.65 GHz), C2-band (7.3 GHz), and C1-band (6.925 GHz). Since both C-bands show a very high degree of similarity ($r \sim 1$), only the C1-band, which is consecutively defined as AMSR2 C-band, was used for this study because it is closer to Sentinel-1 C-band (5.405 GHz). AMSR2 is operated by the Japan Aerospace Exploration Agency (JAXA). This data set provides VOD data at 10 km spatial gridding (native resolution: 62 × 35 km for C-band and 42 × 24 km for X-band (Okuyama & Imaoka, 2015) and an almost daily temporal resolution at this latitude (Jeu & Owe, 2014; Owe et al., 2008). The retrieval is based on the Land Parameter Retrieval Model (LPRM), which uses the τ–ω (tau-omega) radiative transfer model (Mo et al., 1982), which employs a forward modeling approach to retrieve SM, VOD, and surface temperature simultaneously. The employed VOD product is obtained by inverting the 10 km enhanced C-band brightness temperatures (TBs) resulting from their fusion with collocated higher resolution Ka-band TBs using the smoothing filter-based intensity modulation (SFIM) technique (Jeu & Owe, 2014; Liu, 2000; Owe et al., 2008). The second VOD data set, with a spatial gridding of 9 km (native resolution: 36 × 36 km) and a temporal resolution of ~2 days at this latitude, is based on the Soil Moisture Active Passive (SMAP) L-band radiometer sensor (1.4 GHz) operated by

Table 2
Overview of All Employed Remote Sensing (RS) Data sets (AMSR2 = Advanced Microwave Scanning Radiometer 2, LPRM = Land Parameter Retrieval Model, VOD = Vegetation Optical Depth, SMAP = Soil Moisture Active Passive Mission, DCA = Dual Channel Algorithm, MODIS = Moderate Resolution Imaging Spectroradiometer, LAI = Leaf Area Index, CLC = CORINE Land Cover, TCD = Tree Cover Density)

Type of data set	Data set	Main variable(s)	Time period	Temporal resolution/Over pass time (UTC)	Spatial gridding	Reference
Active Microwave RS	Sentinel-1	C-band Backscatter	10/2014–12/2020	~3/6 d, ~05:30 a.m. (desc) ~05:00 p.m. (asc)	10 m	Truckenbrodt, Freemantle, et al. (2019)
Passive Microwave RS	AMSR2	X-, C1-, C2-band VOD (*LPRM*)	10/2014–12/2020	~1.1 d, ~12:00 a.m. (asc)	10 km	Jeu and Owe (2014); Owe et al. (2008)
	SMAP	L-band VOD (*DCA*)	04/2015–03/2020	~1.7 d, ~06:00 a.m. (desc)	9 km	O'Neill, Chan, et al. (2020)
Optical RS	MODIS	LAI (*MCD15A3H*)	10/2014–12/2020	4-day composite	500 m	Myneni et al. (2021)
	MODIS	Surface Reflectance (Band 1, 2, 6) (*MCD19A1*)	10/2014–12/2020	Daily	500 m	Lyapustin and Wang (2022)
Copernicus	CLC 2018	Land Cover Classes	2017–2018	–	100 m	EAA (2019)
	TCD 2018	Tree Cover Density	2018	–	10 m	EAA (2020)

the National Aeronautics and Space Administration (NASA) (O'Neill, Chan, et al., 2020). This data set is retrieved using the renewed Dual Channel Algorithm (DCA), which was renamed from the earlier improved version of the DCA, the Modified Dual Channel Algorithm (MDCA; Chaubell et al., 2020; O'Neill, Bindlish, et al., 2020; O'Neill, Chan, et al., 2020). In the following, we refer to this updated algorithm as "SMAP DCA" instead of the classic DCA or MDCA to align with the terminology used in the SMAP product algorithm theoretical basis document (ATBD). This study utilized the operational NASA SMAP VOD mission product, applying the DCA rather than other algorithms, such as the Multi-Temporal Dual Channel Algorithm (MT-DCA). Like the LPRM, the SMAP DCA algorithm is also based on the τ–ω radiative transfer model (Mo et al., 1982) to retrieve SM and VOD and applies an optimal interpolation method (Backus–Gilbert) to exploit oversampling to provide a spatial gridding of 9 km (Chaubell et al., 2017, 2020; O'Neill, Bindlish, et al., 2020; O'Neill, Chan, et al., 2020).

However, even if both used VOD products have a spatial gridding of 9 and 10 km, this spatial improvement is based on optimal interpolation (SMAP) or the use of higher frequency TBs at higher resolution (AMSR2), they still rely on the native coarse-scale TB data, causing each pixel to represent a spatially mixed signal influenced by adjacent land-cover types (Jeu & Owe, 2014; Owe et al., 2008; O'Neill, Bindlish, et al., 2020; O'Neill, Chan, et al., 2020). Nevertheless, we argue that this is not a substantial limitation because, on the one hand, this study focuses less on spatial variations and more on temporal seasonal patterns and trends of VOD. On the other hand, within the study pixels, the VOD signal should be dominated by the high forest biomass and water content in the Hainich National Park, even for a moderate forest coverage, since forests contribute a much larger proportion of attenuation than smaller land cover types (Chaparro et al., 2021; Jackson & Schmugge, 1991; Jagdhuber et al., 2022; Konings et al., 2019) (Section 2).

Furthermore, the LAI and surface reflectance data sets of the Moderate Resolution Imaging Spectroradiometer (MODIS) sensor onboard the Terra and Aqua satellites were utilized (Lyapustin & Wang, 2022; Myneni et al., 2021) (Table 2). These surface reflectance data sets were used to calculate the normalized difference vegetation and moisture indices (NDVI and NDMI) (Section 3.2). For a comprehensive understanding of the Hainich Forest and its adjacent land cover, the freely and openly accessible CORINE land cover (CLC) 2018 data set and the tree cover density (TCD) 2018 data set of the High Resolution Layer Forest were obtained (EAA, 2019, 2020).

3. Methods

The employed methods can be divided into three stages. In the first part, the physical meaning and preprocessing of SAR data are explained (Section 3.1). Second, based on the in situ and remote sensing data sets (Table 1, Table 2), derived variables (ET and $\mathrm{RWC}_{\mathrm{VOD}}$) and vegetation indices (NDVI and NDMI) were obtained

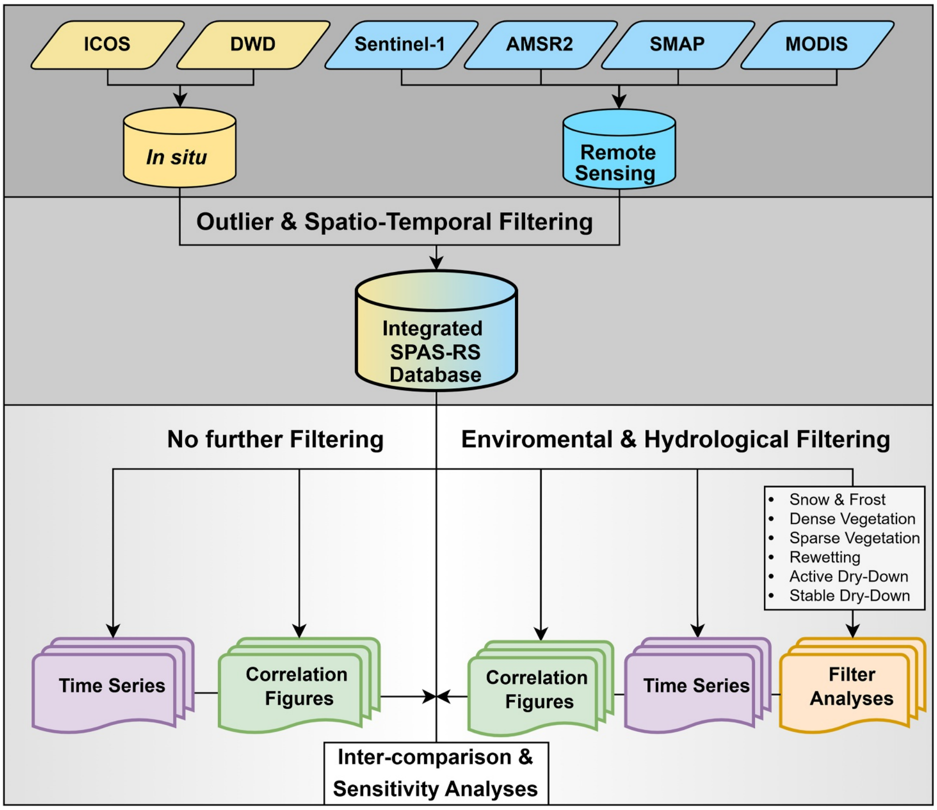

Figure 3. The conceptual workflow of the study includes data curation, filtering, and comparing results (ICOS = Integrated Carbon Observation System, DWD = German Meteorological Service, AMSR2 = Advanced Microwave Scanning Radiometer 2, SMAP = Soil Moisture Active Passive Mission, MODIS = Moderate Resolution Imaging Spectroradiometer, SPAS = soil-plant-atmosphere system, RS = remote sensing).

(Section 3.2). All data sets together form a joint (integrated SPAS-RS) database (Figure 3). Third, this joint database was filtered by environmental and hydrological selection strategies (Section 3.3). This enabled understanding and analyzing the (seasonal) dynamics and the relationship between the SPAS-based variables/proxies and the remote sensing information (RS-based variables). Pearson's correlation coefficient (r) and the Spearman's rank correlation coefficient (r_s) were used as metrics to describe the relationship between variables and measure their sensitivity to varying environmental and hydrologic conditions. In addition, all correlations and slopes were checked for statistical significance using a t-test (Python module ‘scipy.stats‘). Furthermore, a time lag analysis was applied, which estimates the temporal delay between two time series by shifting one series relative to the other and computing their correlation (i.e., cross-correlation) for each shift (i.e., time lag) to identify the lag at which their statistical similarity is maximal. In this study, the time lag analysis was implemented by the ‘statsmodels.tsa.stattools.ccf‘ Python function, based on Brockwell and Davis (2016).

3.1. Physical Meaning and Preprocessing of SAR Data

For the study site, two Sentinel-1 polarization combinations were available: VV denotes the co-polar channel (vertical transmitted and vertical received electromagnetic waves by the SAR sensor) and VH the cross-polar channel (vertical transmitted and horizontal received). The total radar signal received by the SAR sensor (backscatter) over a vegetated surface is a composite of scattering produced by the canopy (vegetation volume scattering), scattering caused by the underlying surface attenuated by the vegetation (soil scattering), and additional scattering generated by soil-vegetation interactions (Ulaby et al., 1986). Physically, the cross-polarized backscatter (VH) occurs when the incident polarization is changed by the target (depolarization) due to structural randomness and volume interactions (e.g., leaves and twigs). In contrast, co-polarized backscatter (VV) largely preserves the transmitted polarization (no depolarization) and is sensitive to surface and double-bounce scattering (Freeman & Durden, 1998). Therefore, VH backscatter appears more sensitive to vegetation volume scattering in deciduous broadleaf forests, as it is more sensitive to multiple, randomly oriented scatterers in the canopy forests, like leaves and twigs (Ling et al., 2022; Proietti et al., 2020; Rüetschi et al., 2019; Soudani et al., 2021). In addition, several studies have shown that in deciduous broadleaf forests, the Sentinel-1 VH backscatter decreases with the onset of the foliage (leaf-on conditions) and thus with increasing leaf biomass (Dostálová et al., 2018; Dubois et al., 2020; Frison et al., 2018; Ling et al., 2022; Rüetschi et al., 2019; Soudani et al., 2021).

All Sentinel-1 scenes were processed to a radiometrically terrain-corrected (RTC) data set by utilizing the Python module pyroSAR (Truckenbrodt, Cremer, et al., 2019). This includes the radiometric calibration to gamma nought (γ^0) to account for a vegetation volume scattering target like the Hainich Forest (Ulaby et al., 1986), multi-looking to 10 m pixel spacing, radiometric terrain flattening, and geocoding. In this process, an aerial laser scanning (ALS) digital elevation model (DEM) based on the 50th percentile of vertical vegetation height of the Hainich National Park was utilized (Zehner et al., 2023). According to Zehner et al. (2023), this 50th percentile ALS DEM resulted in more homogeneous backscatter between orbits compared to other DEMs. Furthermore, the available two orbits at the same time of day were merged for the ascending (~05:00 p.m. UTC, evening) and descending (~05:30 a.m. UTC, morning) flight directions to increase the temporal resolution up to ~3 days for 09/2016–12/2021.

3.2. Retrieval of Variables and Indices

On the one hand, SM, RH, VPD, and ET, calculated from LE, were used from in situ measurements at the ICOS station. On the other hand, LAI, NDVI, and NDMI were retrieved from optical remote sensing. In addition, microwave VOD data were converted to RWC_{VOD}. A schematic overview of these data, along with the corresponding remote sensing sensors and the SPAS, is shown in Figure 4.

Evapotranspiration (ET). The ET rate, expressed in mm d^{-1}, was calculated from the latent heat (LE), given in J $\text{m}^2\ \text{s}^{-1}$, by dividing LE by the latent heat of vaporization or evaporation (λ), expressed in MJ kg^{-1} (Nobel, 2020). The latent heat of vaporization represents the amount of energy required to convert a certain mass of water from liquid to water vapor. According to Allen et al. (1998), the λ depends on the air temperature (TA) expressed in °C. In this study, as is also commonly assumed, the TA was set to 20°C to calculate ET, corresponding to $\lambda = 2{,}454$ MJ kg^{-1} (Allen et al., 1998).

Relative water content (RWC). VOD can be directly converted into RWC by normalizing VOD, under the assumption that RWC is not dependent on the phenological changes of the dry biomass of vegetation (Jagdhuber et al., 2022; Martínez-Vilalta et al., 2019; Rao et al., 2019), and temperature (Zhao et al., 2024). However, this assumption does not hold during periods of rapid biomass and plant structure changes (Martínez-Vilalta et al., 2019). Hence, one way of estimating RWC directly from VOD is to consider only time periods where the dry biomass and plant structure of vegetation can be assumed effectively constant (Hellwig et al., 2023).

For the study site, based on site-specific vegetation images taken regularly (approximately biweekly), in situ data, and vegetation indices, it is assumed that from DOY 130 to 250, the dry biomass and the plant structure of vegetation, and the temperature did not change considerably. Hence, following Rao et al. (2019), RWC_{VOD}, expressed in %, was calculated by normalizing VOD:

$$\text{RWC}_{\text{VOD}} = \frac{\text{VOD} - \text{VOD}_{\text{min}}}{\text{VOD}_{\text{max}} - \text{VOD}_{\text{min}}} \times 100\,. \tag{1}$$

The minimum and maximum of VOD were determined using the 5th and 95th percentiles to reduce high-frequency noise (Rao et al., 2019). For this, the period from DOY 130 to 250 for 2015 to 2019 was considered (Hellwig et al., 2023):

$$\text{VOD}_{\text{min}} = P_5\left(\text{VOD}_{\text{DOY 130–250 (2015–2019)}}\right), \tag{2}$$

$$\text{VOD}_{\text{max}} = P_{95}\left(\text{VOD}_{\text{DOY 130–250 (2015–2019)}}\right). \tag{3}$$

However, RWC_{VOD} cannot be directly compared with physically measured in situ RWC without information about the absolute water content. Therefore, RWC_{VOD} varies between ~0% and ~100% by design (normalization), which

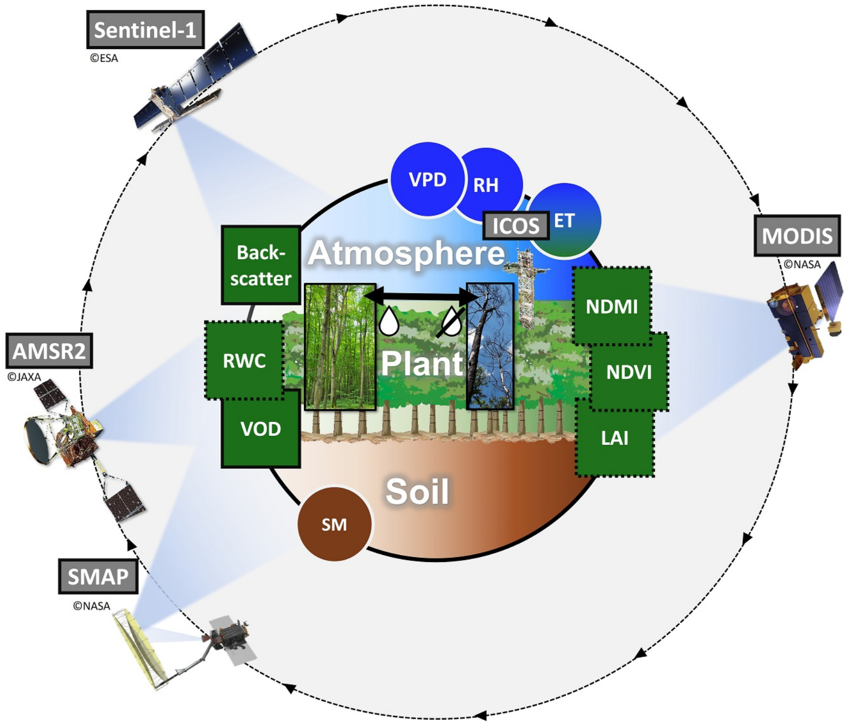

Figure 4. Schematic representation of the SPAS monitoring under drought and non-drought conditions, including the considered remote sensing and in situ time series data (VPD = vapor pressure deficit, RH = relative air humidity, ET = evapotranspiration, NDMI = normalized difference moisture index, NDVI = normalized difference vegetation index, LAI = leaf area index, SM = soil moisture, VOD = vegetation optical depth, RWC = relative water content of vegetation; ©ICOS photo: Marlin Müller). SPAS-based variables (i.e., SM, ET, RH, VPD; white circle) were measured in situ, while SPAS-based proxies (i.e., LAI, NDVI, NDMI, RWC_{VOD}; black dashed square) and RS-based variables (i.e., VOD, backscatter; black square) were estimated or provided by RS. The drought and non-drought conditions were displayed schematically by drops and representative in situ images of the Hainich Forest.

is beyond the expected physiological values. Thus, we refer to this metric as effective RWC_{VOD}, as it is estimated directly from RS-based VOD. Nevertheless, RWC_{VOD} enables drought-based evaluations (Rao et al., 2019), which are possible across sensors and years due to the normalization. This makes RWC_{VOD} an efficient drought indicator.

Normalized difference vegetation and moisture indices (NDVI and NDMI). The MODIS surface reflectance data set was used to derive the NDVI and NDMI indices. The NDVI was calculated following Tucker and Sellers (1986) using band 1 (Red) and band 2 (NIR) of the MODIS sensor, and the NDMI was calculated according to the United States Geological Survey (2023) by using band 2 (NIR) and band 6 (SWIR).

Standardized Precipitation Index (SPI). A widely used indicator for identifying hydrological conditions based solely on precipitation is the SPI, which was initially proposed by McKee et al. (1993) to quantify the severity of droughts for different time periods. In this study, the 12-month SPI (SPI-12), based on local rain data, was calculated to identify hydrological droughts (from $SPI < 0$ to $SPI \geq 0$, including $SPI \leq -1$) and to classify wet ($SPI \geq 1$) or dry ($SPI \leq -1$) years after McKee et al. (1993) and WMO (2012). The SPI-12 implies that the precipitation of 12 consecutive months is compared to the same consecutive months of all available years. The maximum absolute value, while preserving the original sign of each year, under effectively constant vegetation conditions (DOY 130–250), was used to classify each year, further called $SPI\text{-}12_{Indicator}$.

3.3. Filtering and Selection Strategies

Various filters were developed and applied to understand the behavior of remote sensing and SPAS under different climatic conditions (Figures 3 and 4). These filters can be divided into four categories: outlier, spatio-temporal, environmental (snow and frost, dense and sparse vegetation), and hydrological (rewetting, active dry-down, and stable dry-down) (Table S1 in Supporting Information S1). For the sake of consistency, we use the term “filter” to refer not only to classical filtering but also to the selection of certain environmental and hydrological conditions.

Outlier filtering. In the first filtering step, data values were manually checked for plausibility to remove incorrect values resulting from sensor errors. In addition, a percentile filter ($P_{2.5}$ and $P_{97.5}$) was applied over time to the Sentinel-1 data to remove outliers.

Spatial filtering. In the second step, the remote sensing data were spatially filtered. The optical remote sensing data sets were clipped to the spatial extent of the corresponding microwave remote sensing data and aggregated using a mean filter. The Sentinel-1 data were clipped to match the area around the ICOS station (50 × 50 m) and aggregated using a mean filter. Although the footprint of the eddy covariance in situ measurements (annual climatology) has a radius of about 500 m around the tower (Anthoni et al., 2004; Klosterhalfen et al., 2023), the Sentinel-1 data were only spatially averaged over 50 × 50 m to obtain the highest possible spatial resolution. This is a reasonable compromise between maintaining the maximum spatial resolution of the Sentinel-1 data (pixel spacing: 10 × 10 m) and reducing SAR-related inherent speckle noise, while the temporal filtering does not have to be as high as it would be without spatial filtering.

Temporal filtering. A Savitzky-Golay filter with a window of 31 days was chosen to smooth the time series and extract monthly and seasonal patterns. This filter employs the least squares method to fit data points to a polynomial, reducing high-frequency components without removing them. The filter thus preserves essential distribution properties, such as minimum, maximum, and deviation (Luo et al., 2005; Savitzky & Golay, 1964). All data were linearly interpolated to a daily basis before applying the filter to ensure a perfect temporal match, as the remote sensing data have different temporal resolutions (Table 1, Table 2).

Frost and snow filtering. Based on Benninga et al. (2019), a filter was developed that excludes snow and frost conditions when the TA (measured at a height of 200 cm) is below 1°C (Table S1 in Supporting Information S1). To further improve the reliability of this filter, the data were also excluded when the TS at 2 cm soil depth was below 1°C. Unlike all in situ data, which are daily averages, the reference for TA and TS was chosen as the time immediately before the Sentinel-1 acquisitions (Table 2).

Vegetation density filtering. In addition to the five vegetation phenological phases (Figure 2), which remain constant throughout the entire study period, a more detailed filtering was designed to account for the sensitivity of microwaves to varying vegetation densities. Since high-frequency active and passive microwaves strongly interact with dense vegetation (Bauer-Marschallinger et al., 2019; Konings et al., 2021; Steele-Dunne et al., 2017), a filter using LAI as a proxy for vegetation density was developed to divide the study period into sparse and dense vegetation phases (Table S1 in Supporting Information S1). Since the understory in the Hainich Forest develops before the beech canopies are greened (Figure 2), a LAI value of 2 $m^2\ m^{-2}$ was selected as a threshold based on in situ data and vegetation images. The sparse vegetation (mask) filter ($LAI \leq 2$) screens out sparse vegetation conditions to ensure that only the dense vegetation phase corresponds to periods of full canopy coverage (leaf-on conditions). Accordingly, the dense vegetation (mask) filter ($LAI > 2$) screens out dense vegetation and only leaves sparse vegetation (leaf-off conditions). Instead of using LAI, a DOY filter could also be used to determine these conditions, thereby reducing confounding in subsequent analyses.

Hydrological filtering. For this study, hydrological selection strategies were developed that split the data into wet and dry conditions. Thus, the drying, rewetting, and infiltration processes, which are fundamental hydrological processes within the SPAS, can be analyzed separately over time. Additionally, the influence of precipitation on electromagnetic microwaves, such as the increase in backscattering (Benninga et al., 2019), intercepted water (Jong, 2000), or changed leaf orientation (Jackson & Moy, 1999), can be filtered.

The hydrological selection strategies are based on hourly precipitation amounts of the DWD weather station (DWD, 2021). First, if more than 1 mm of rain falls in 1 hour or over several continuous hours, these consecutive hours are defined as precipitation events (Table 3). Alternatively, 0.5 mm of rain may also be considered as the precipitation threshold, provided that a total of more than 1 mm of rain has fallen in the last 24 hr. This includes the case, for instance, where two precipitation events occur in a short sequence, each with an amount of less than 1 mm. Second, the hydrological phases were defined according to the time following the precipitation events. The rewetting phase includes the time of the precipitation event plus 24 hr afterward (infiltration phase), determined according to Mein and Larson (1973). The following 72 hr were classified as active dry-down, and the time after

Table 3
Definition of Hydrological Events, Phases, and Terms Based on Bender and Schaller (2012) and Mein and Larson (1973)

Hydrological processes		Definition
Hydrological Event	Precipitation Event	≥1 mm per continuous hour of rain ≥0.5 mm per continuous hour of rain and ≥1 mm within the last 24 hr
Hydrological Phase	Rewetting	start to end of precipitation event plus 24 hr
	Active Dry-Down	end of the rewetting phase plus 72 hr
	Stable Dry-Down	end of the active dry-down phase until the beginning of the next precipitation event
Hydrological Term	Heavy Rain	≥10 mm per continuous hour of rain
	Continuous Rain	≥5 mm per continuous hour of rain and ≥6 hr of continuous rain
	Normal Rain	not heavy or continuous rain

that until the start of the next precipitation event as stable dry-down. Third, since precipitation events vary widely in duration and intensity, these events were divided into heavy, continuous, and normal rain after Bender and Schaller (2012).

4. Results

4.1. Hydrological Conditions and Variables of the Soil-Plant-Atmosphere System

According to the $\text{SPI-12}_{\text{Indicator}}$ (Section 3.2) for the reference period (2014–2020), except for 2017 ("very wet") and 2020 ("near normal"), all other years were "very dry" or "extremely dry" (Table S2 in Supporting Information S1). In particular, the years 2017 and 2018 exhibited contrasting hydrological conditions. Thus, these years are analyzed in more detail in the following.

Figure 5 shows the amount of precipitation per hourly continuous rain event divided into different classes and hydrological phases between May and September of 2017 and 2018, respectively. The summer of 2017 experienced numerous high precipitation events ($\sum = 359$ mm) characterized by primarily continuous rainfall, whereas the summer of 2018 experienced a severe lack of precipitation ($\sum = 54$ mm). In 2018, stable dry-down phases were dominant (~43% of the time), whereas they were less common in 2017 (~27% of the time). Precipitation fell at regular intervals in the summer of 2017, resulting in only short dry-down phases (~54 hr on average). In contrast, the summer of 2018 was characterized by very long dry-down periods (~181 hr on average), with up to 14 days without rain.

These hydrological differences are also reflected in the selected SPAS-based variables/proxies. Figure 6 illustrates the temporal series of $SM_{\text{-8cm}}$, ET, and TA, as well as the vegetation indices NDMI, LAI, and NDVI in 2017 and 2018 during different vegetation phases. In the very wet year 2017, $SM_{\text{-8cm}}$ decreased at the beginning of the vegetation period in March and increased at the end of the vegetation period in September (Figure 6a), remaining above 30 vol. % even in summer. In contrast, in the extremely dry year 2018, $SM_{\text{-8cm}}$ decreased strongly from a very high level (~44 vol. %; black arrow) from April to September (~17 vol. %; orange arrow) and did not begin to recover before mid-November, while in the previous year, $SM_{\text{-8cm}}$ had already returned to the winter level (~42 vol. %) by then.

ET increased with the phenological reactivation phase, reaching its peak depending on the hydrological conditions (Figure 6b). In the extremely dry year 2018, ET increased 1 month earlier (black arrow) and already peaked in May (~1.7 mm d^{-1}) compared to a peak in August (~2.7 mm d^{-1}) during the very wet year 2017 (orange arrow). In late summer, ET typically returns to its winter level in October/November. The vegetation indices (NDMI, LAI, NDVI) accurately reproduce the phenology, reaching their maximum in May/June (Figures 6d–6f). In 2018, the LAI increase started one month earlier (April; black arrow), and the NDMI and NDVI were strongly reduced during the low foliage phase (orange arrow). In addition, the TA_{95} rose during the vegetation period from around 7°C in March to 23°C in August, and then dropped back to 7°C in November (Figure 6c). Compared to 2017, the TA_{95} also increased one month earlier (April; black arrow) and was abnormally high during the summer of 2018, especially in August (~27°C; orange arrow).

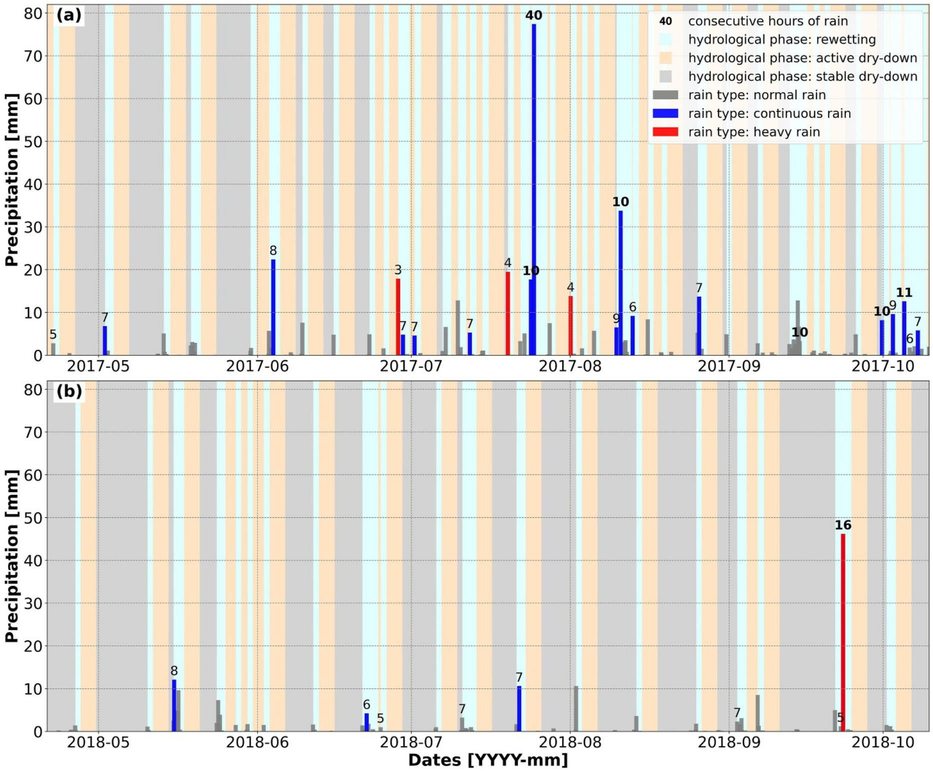

Figure 5. Total precipitation per hourly continuous rain event, divided into different rain types and hydrological phases between May and September (a) 2017 and (b) 2018 of the German Meteorological Service (DWD) station "Hörselberg-Hainich-Behringen". If rain fell for at least 5 hours continuously or if there was a heavy rain event, the number of total hours per event is shown above the corresponding precipitation bar. See Table 3 for the description of the precipitation events and hydrological phases.

4.2. Microwave Data and Variables of the Soil-Plant-Atmosphere System

Figure 7 and Figure S1 in Supporting Information S1 illustrate the active microwave remote sensing time series in combination with selected SPAS-based variables/proxies. In the following, we will focus on the Sentinel-1 ascending (evening) acquisitions (05:30 a.m. UTC) instead of the descending (morning) acquisitions (05:00 p.m. UTC) to exclude any dew effects on the SAR signal. Nevertheless, the descending (morning) acquisitions were also analyzed.

As shown in Figure 7, the S-1 $\gamma_{VH}^{evening}$ peaked in March/April (∼−12 dB), then decreased until June (∼−13.5 dB), fluctuated during the summer, and decreased again in September/October (∼−14 dB). During the winter, the S-1 $\gamma_{VH}^{evening}$ returned to the spring level (∼−12 dB). Additionally, a significant slight decrease can be observed over the years (ΔS-1 $\gamma_{VH}^{evening} \sim -0.1$ dB per year). Comparing the S-1 $\gamma_{VH}^{evening}$ with the LAI, an anti-correlation is observed (Pearson correlation coefficient $r = -0.71$, Spearman's rank correlation coefficient $r_s = -0.66$), particularly noticeable during the very wet year 2017 ($r = -0.93$, $r_s = -0.93$) (Figure 7a). This negative correlation, decreasing S-1 $\gamma_{VH}^{evening}$ with increasing LAI, indicates a contrasting and negative coupled process. The same contrasting relationship is observed for ET ($r = -0.48$, $r_s = -0.5$) and VPD ($r = -0.51$, $r_s = -0.51$; Figures 7c and 7d). On the contrary, SM_{-8cm} and S-1 $\gamma_{VH}^{evening}$ are positively correlated ($r = 0.70$, $r_s = 0.71$), especially at the beginning and end of the vegetation period (Figure 7b), indicating decreasing S-1 $\gamma_{VH}^{evening}$ with decreasing SM_{-8cm}, and a synchronous and coupled process. Due to the very high similarity of r and r_s, the focus of further analyses will be exclusively on r unless significant differences are found.

The corresponding r values between all variables are shown in Figure 8. Generally, the absolute correlations between S-1 $\gamma^{evening}$ and all listed SPAS-based variables/proxies are much higher for the VH polarization ($|r| \sim 0.59$ on average) than the VV polarization ($|r| \sim 0.33$ on average). In general, for deciduous broadleaf forests, vegetation volume scattering is essential, to which the VH backscatter is more sensitive, compared to soil

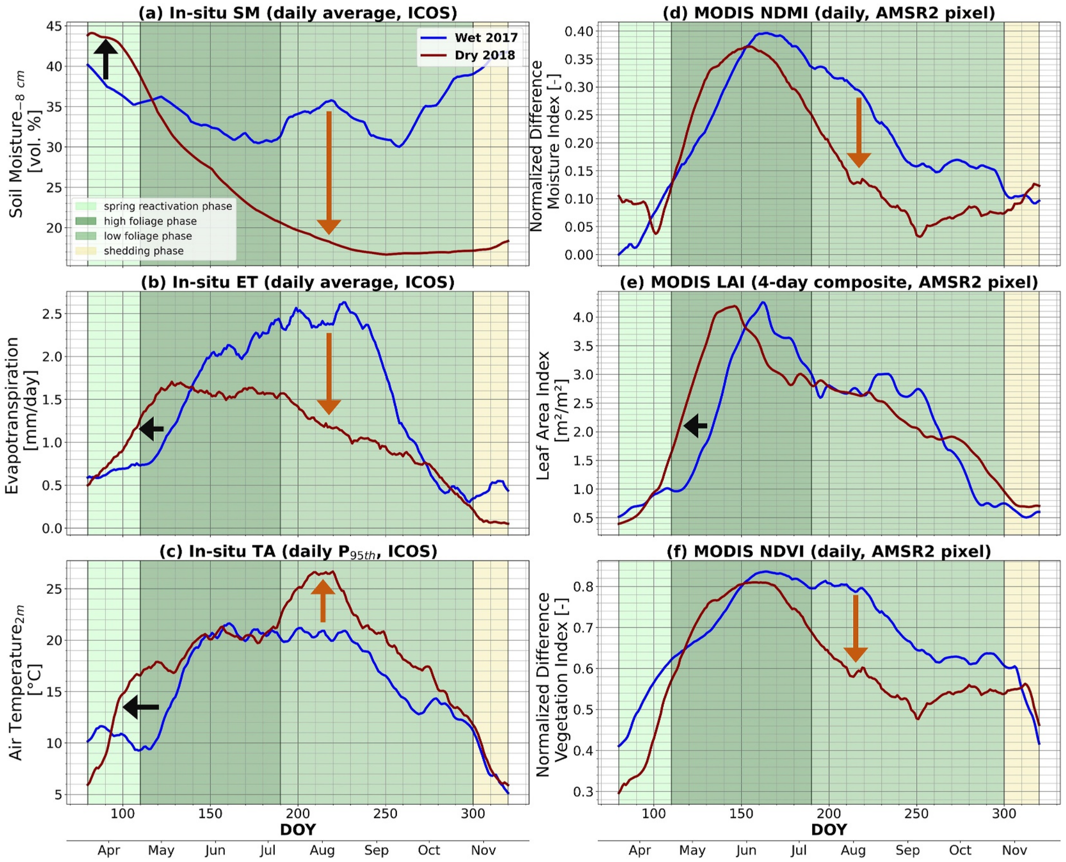

Figure 6. Time series of (a) daily in situ soil moisture (SM) from 8 cm soil depth, (b) daily in situ evapotranspiration (ET), (c) daily 95th percentile of in situ air temperature (TA_{95}) in 2 m height from the "DE-Hai" ICOS station, as well as (d) daily normalized difference moisture index (NDMI), (e) 4-day composite of leaf area index (LAI), and (f) daily normalized difference vegetation index (NDVI), adapted after Hellwig et al. (2023). The vegetation index data were clipped to the spatial extent of the microwave data (in this case, to AMSR2). The time series was shortened to the vegetation phases (DOY 80–320). The different years were colored according to their hydrological conditions based on the SPI-$12_{\text{Indicator}}$ (red for dry and blue for wet conditions; Table S2 in Supporting Information S1) and the background according to the respective vegetation phase (light green to yellow; Section 2.1, Figure 2). The main differences between the years are indicated by arrows (black arrow: saturated moisture level and earlier start of the vegetation period; orange arrow: drought-dependent reduction in moisture and vegetation; Section 5.1).

scattering, to which the VV backscatter is more sensitive (see Section 3.1). Therefore, we will primarily focus on the VH polarization in the following. The correlations between LAI and ET ($r = 0.85$), LAI and VPD ($r = 0.85$), VPD and RH ($r = -0.84$), as well as ET and VPD ($r = 0.81$) are also very high, indicating the influence of third variables on the relationship between backscatter and SPAS-based variables/proxies. SM_{-8cm} correlates most with LAI ($r \sim 0.61$ on average).

A sensitivity analysis was performed to study the impact of each filter combination on these results under varying hydrological conditions. Figure 9 shows the selected filter combination that improves the correlation compared to the reference data (temporally aggregated data) between S-1 $\gamma_{VH}^{\text{evening}}$ and SPAS-based variables/proxies. Under wet conditions, filtering frost and snow constantly improves the correlations ($|\Delta r| \sim 0.07$ on average). In addition, combining a hydrological filter (i.e., different atmospheric saturation states) with the frost and snow filter is beneficial ($|\Delta r| \sim 0.09$ on average) to achieve the highest significant correlations for VPD ($r = -0.76$), ET ($r = -0.89$), and LAI ($r = 0.95$). Regarding these filter combinations, no filter stands out for all SPAS backscatter combinations. Under extremely dry conditions, applying the rewetting phase (selection) filter with the snow and frost filter improves the correlations ($|\Delta r| \sim 0.08$ on average). In addition, applying the dense vegetation (mask) filter, especially for stable dry-downs, leads to an inversion of the relationship between ET and VPD, resulting in a considerable improvement ($|\Delta r| \sim 0.26$ on average) with the highest significant correlations for SM ($r = 0.91$).

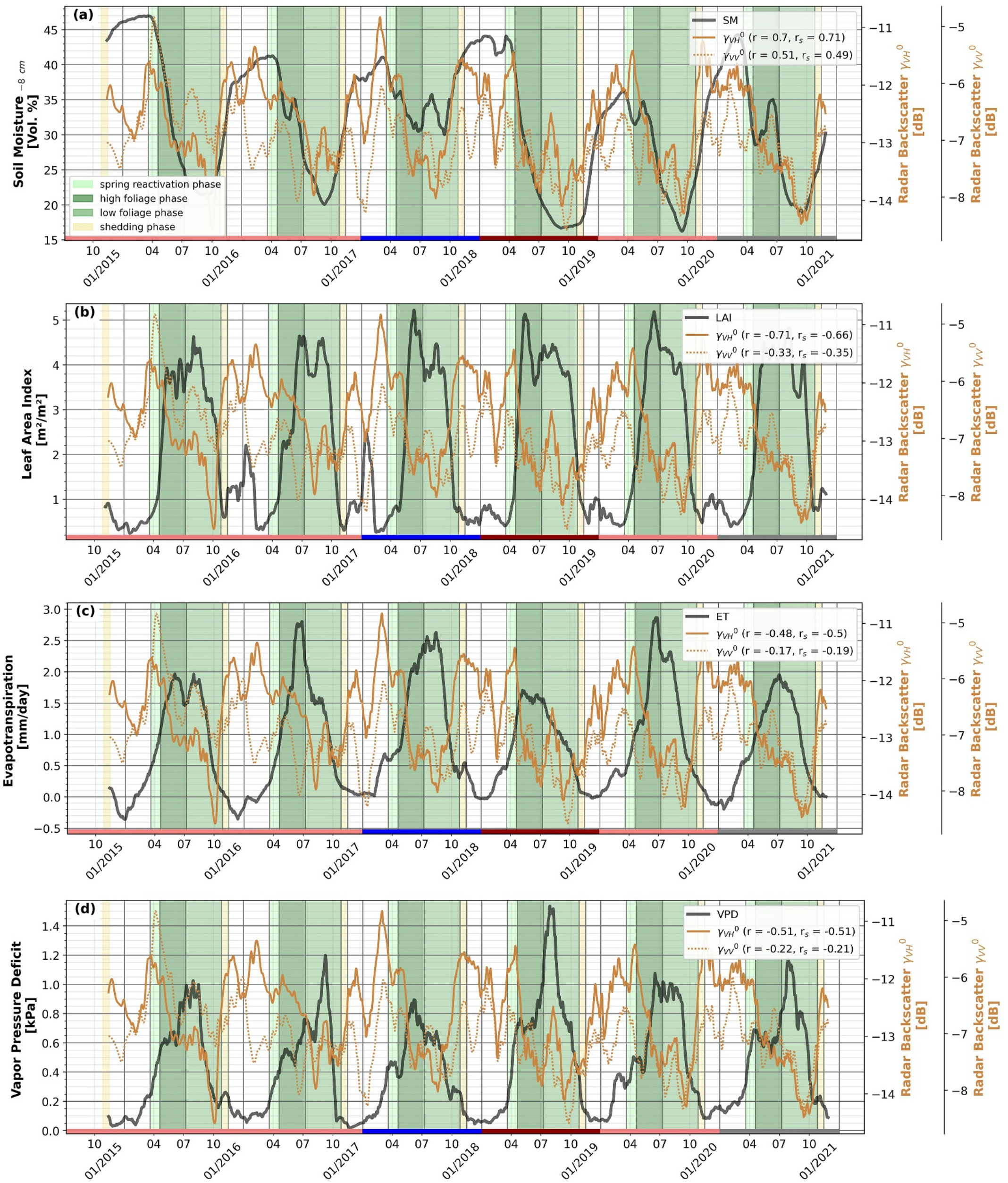

Figure 7. Time series of aggregated Sentinel-1 C-band ascending (evening) VV- and VH- polarized backscatter (S-1 γ^{evening}) and (a) daily in situ soil moisture (SM) from 8 cm soil depth, (b) 4-day composite of leaf area index (LAI), (c) daily in situ evapotranspiration (ET), and (d) daily in situ vapor pressure deficit (VPD) from the "DE-Hai" ICOS station (50 m × 50 m) for the time period 10/2014 to 12/2020. The LAI data were clipped to the spatial extent of the Sentinel-1 data. To improve understanding and interpretation, the time series have been smoothed with the Savitzky-Golay filter (window size = 31 days). r gives the Pearson and r_s the Spearman's rank correlation coefficient between the variable and the backscatter time series, respectively, with all values being significant to a p-value of 0.001. Exceptions are marked with ×. The background was colored according to the respective vegetation phase (light green to yellow; Section 2.1, Figure 2), and the short bars above the *x*-axis indicate the hydrological conditions of the respective years based on the SPI-12$_{\text{Indicator}}$ (red for dry, blue for wet, and gray for normal conditions; Table S2 in Supporting Information S1).

However, screening out dense vegetation does not play an essential role under very wet conditions (Figure S2 in Supporting Information S1).

Figure 10 illustrates the VOD from passive microwave remote sensing and the calculated RWC$_{\text{VOD}}$ from 2017 to 2019.

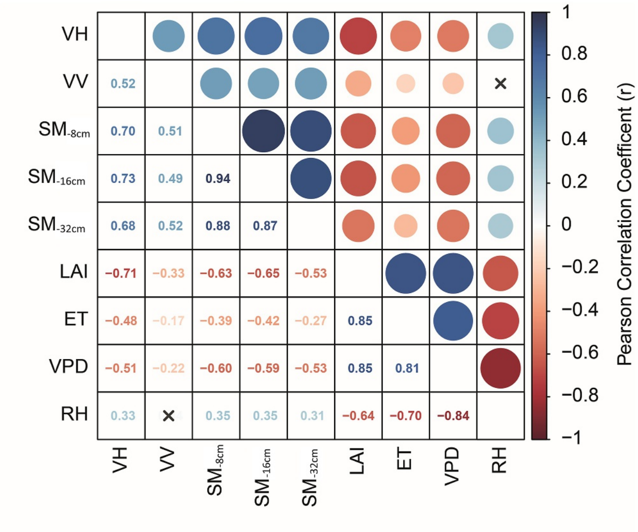

Figure 8. Pearson correlation coefficient (r) for the temporally aggregated Sentinel-1 C-band ascending (evening) VV- and VH- polarized backscatter (S-1 γ^{evening}) and in situ soil moisture from different soil depths ($\text{SM}_{\text{-8cm}}$, $\text{SM}_{\text{-16cm}}$, $\text{SM}_{\text{-32cm}}$), leaf area index (LAI), in situ evapotranspiration (ET), in situ vapor pressure deficit (VPD), and in situ relative humidity (RH) for the study period (10/2014-12/2020) without using environmental filters. All values are significant to a p-value of 0.001. Exceptions are marked with ×.

As expected, the attenuation of land emission at the X- and C-bands is clearly higher (VOD ~ 0.85) than at the L-band (VOD ~ 0.6) (Figures 10a–10c). Since RWC_{VOD} cannot be directly compared with in situ RWC (Section 3.2), in the following, we will focus less on absolute values and more on relative changes and comparisons between sensors and years. In general, RWC_{VOD} increases strongly from March (spring reactivation phase) to May/June (high foliage phase) and drops considerably in July/August (low foliage phase) before increasing again (Figures 10d–10f). It is noticeable that the annual signal of VOD and RWC_{VOD} is comparable for all three wavelengths. In terms of different hydrological conditions, the X-band RWC_{VOD} is considerably increased during the low foliage phase under very wet conditions (2017; ~30% on average) compared to extremely dry conditions (2018; ~0% on average) (Figure 10d). This positive difference for X-band (~50%) is lower for C-band (~10%) and even negative for L-band (~−30%) in July (Figures 10e and 10f). Notably, during very wet conditions (2017), a second weaker RWC_{VOD} peak (RWC_{VOD} = ~20–40%) occurs during autumn (DOY ~250), compared to the first RWC_{VOD} peak (RWC_{VOD} = ~80%).

The highest correlation coefficients are found among the RWC_{VOD} at different frequencies (Figure 11). The closer the frequencies, the higher the r. For example, the X-band RWC_{VOD} is more similar to the C-band RWC_{VOD} (r = 0.97) than the L-band RWC_{VOD} (r = 0.86). For the three different vegetation indices, it is noticeable that the X-band RWC_{VOD} correlates more strongly with the NDVI (r = 0.84) than with the LAI (r = 0.73), while the L-band RWC_{VOD} correlates more strongly with the LAI (r = 0.77) than with the NDVI (r = 0.74). There is no clear dominance for C-band RWC_{VOD}. In this context, the NDMI appears less related to RWC_{VOD} (r ~ 0.53 on average). Overall, the C-band RWC_{VOD} shows the highest correlations with all three indices and ET (r = 0.8). As expected, L-band RWC_{VOD} exhibited the highest anti-correlation with $\text{SM}_{\text{-8cm}}$, albeit at a relatively low level (r = −0.34).

5. Discussion

To enhance our understanding of forest water dynamics, we interpret multi-year droughts and vegetation responses in the Hainich Forest using SPAS-based variables/proxies (Section 5.1). Based on this, we discuss how active-passive microwave-derived RWC and backscatter can track these forest water dynamics to evaluate their potential and limitations (Sections 5.2, Section 5.3).

5.1. Water Dynamics in a Temperate Deciduous Broadleaf Forest During Drought and Non-Drought Years

The 2018–2020 multi-year drought was an exceptional event compared to past droughts in Central Europe (Bastos et al., 2020; Buras et al., 2020; Marx, 2022; Rakovec et al., 2022) and severely affected forests in Germany (Thonfeld et al., 2022). In Thuringia, more than one-third of all beeches suffered from drought damage in 2020 (35.6%), including the stands in the Hainich Forest (TMIL, 2022). Here, wet conditions in 2017 and during the spring of 2018 had refilled water reservoirs by the beginning of the drought period ($\text{SM}_{\text{-8cm}}$ ~44 vol. %, Figure 6a, black arrow). Combined with a sunny (DWD, 2019) and a warm April (TA_{95} ~ 15°C, Figure 6c, black arrow), the vegetation period started earlier than usual. Accordingly, LAI and ET increased on average 20 days earlier, from DOY ~100, compared to 2017 (Figures 6b and 6e, black arrows).

Following on, the early season start, early growth, and ET increase exacerbated the impact that the subsequent summer drought had on the forest ecosystem due to the anticipated water uptake from the soil and its release to the atmosphere (Bastos et al., 2020). In the Hainich Forest, the SM depletion was rapid: The depletion rate was more than doubled between 2017 and 2018 ($\Delta\text{SM}_{\text{-8cm}}$ ~ −0.9 to ~ -2.3 vol. % per 10 days between DOY 100 to 150; Figure 6a). Moreover, this quick SM depletion was further intensified. This was caused by constantly high temperatures (Figure 6c), very long sunshine duration (~10–11 hr d^{-1}) due to less cloud cover in June 2018 (DWD, 2019), and prolonged dry-down phases without precipitation, lasting an average of 181 hr (~8 days)

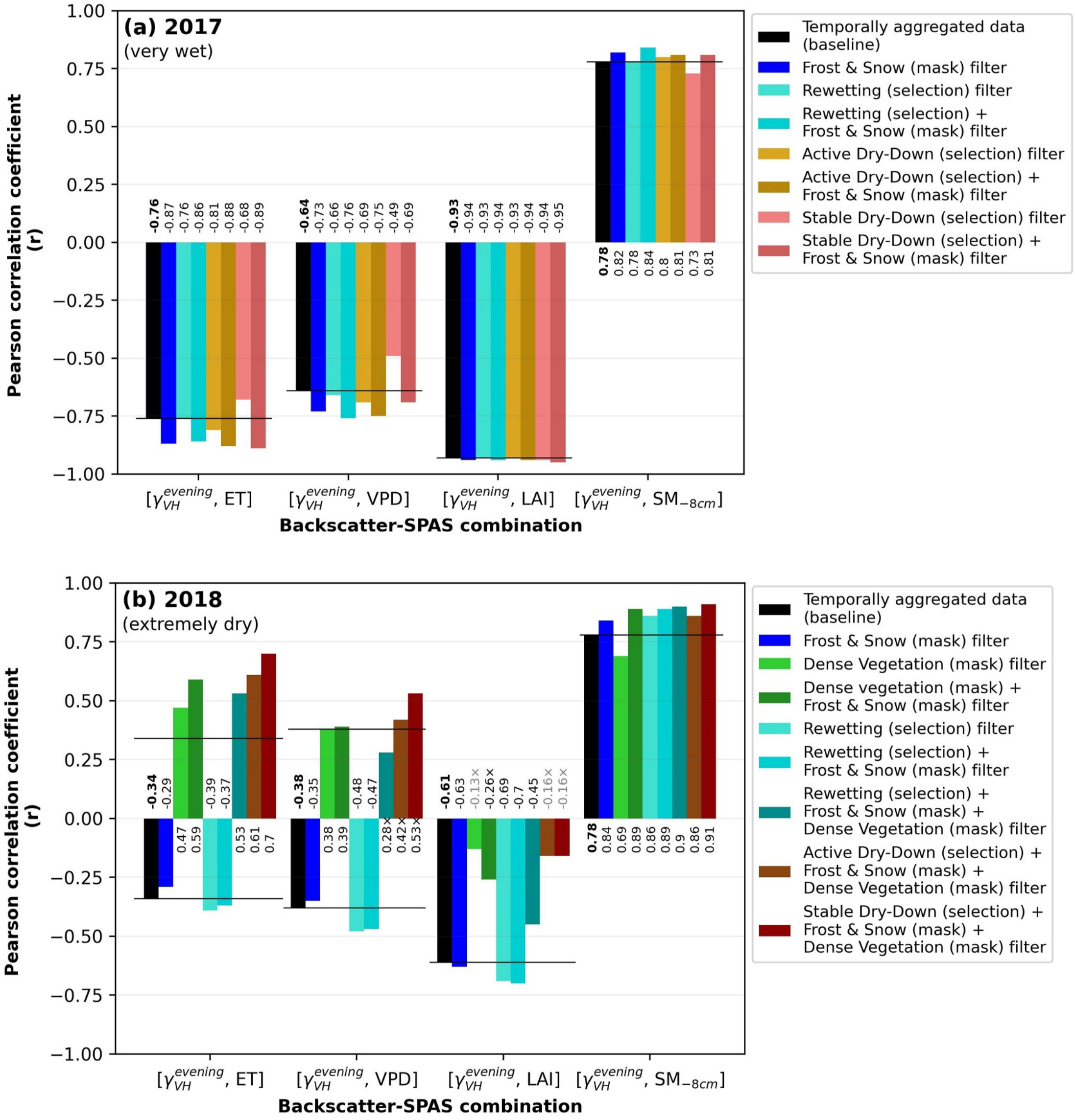

Figure 9. Comparison of selected filter combinations showing an improvement of the Pearson correlation coefficient (r) compared to the reference data (temporally aggregated data; black lines across all bars) between Sentinel-1 C-band ascending (evening) VH-polarized backscatter S-1 ($\gamma_{VH}{}^{evening}$) and in situ evapotranspiration (ET), in situ vapor pressure deficit (VPD), leaf area index (LAI) as well as in situ soil moisture (SM) from 8 cm soil depth) for (a) 2017 and (b) 2018. All values are significant to a p-value of 0.001. Exceptions are marked with an × ($0.001 < p < 0.05$) or are completely grayed out ($p \geq 0.05$). The remaining filter combinations are shown in Figure S2 in Supporting Information S1.

(Figure 5b). These long dry-down phases are particularly harmful to the Hainich Forest as the beeches depend on summer precipitation, since the winter water reservoir can quickly be depleted by the middle of summer (TMIL, 2022).

In July 2018, ET was considerably lower (~1.6 mm d^{-1}) and began to decline two months earlier (July) than in the previous very wet year (~2.6 mm d^{-1}, Figure 6b). This was caused by extremely dry atmospheric conditions ($RH < 30\%$, $VPD > 1.5$ kPa, $TA_{95} > 26°C$, Figure S1c in Supporting Information S1, Figures 6c and 7d, orange arrow), which led to shortened water resources in the already shallow main root area of the beeches on porous limestone, with drastically low shallow SM_{-8cm} (<20 vol. %, Figure 6a, orange arrow), especially at slightly deeper layers ($SM_{-32cm} < 28$ vol. %, Figure S1b in Supporting Information S1). Under these water stress conditions, beeches adjust their hydraulic behavior to respond by closing their stomata early, minimizing water loss through transpiration and, ultimately, preventing leaf desiccation (Konings et al., 2021; Lambers &

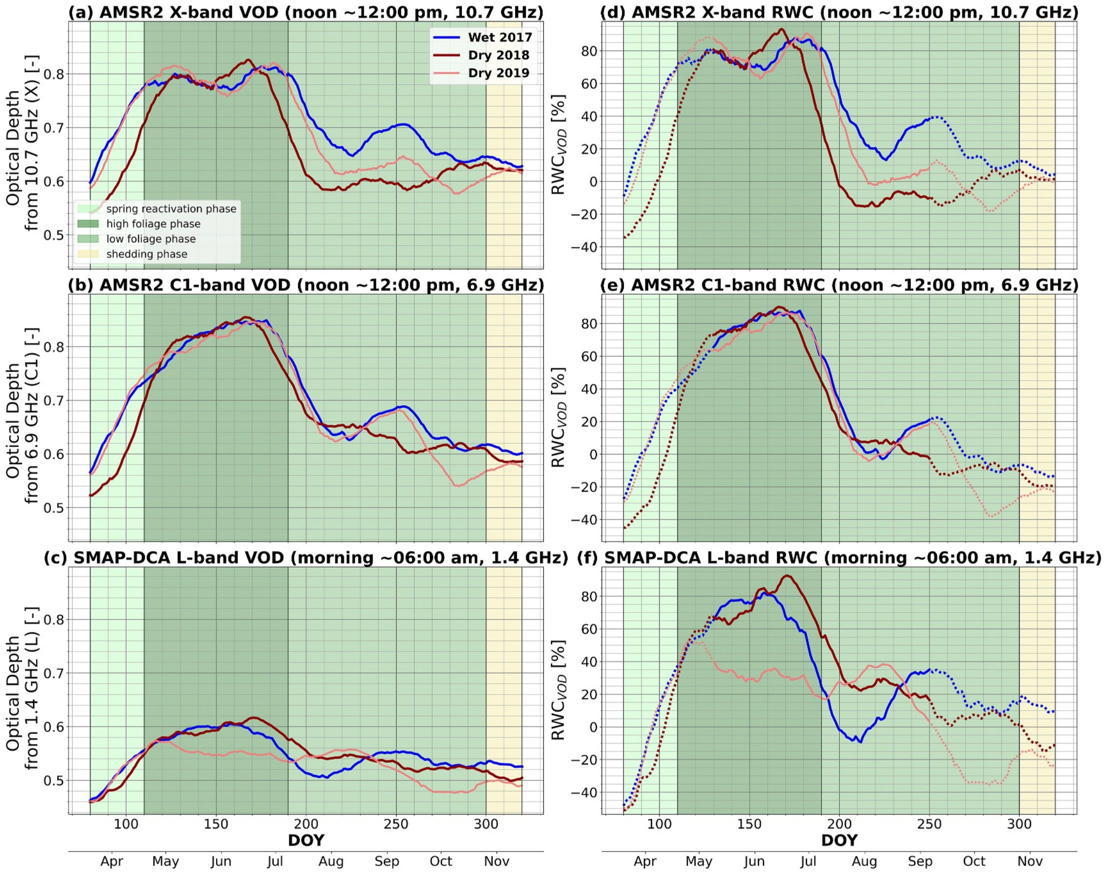

Figure 10. Time Series of (a–c) vegetation optical depth (VOD) and (d–f) relative water content (RWC_{VOD}) derived from AMSR2 X- and C1-band and SMAP DCA L-band, adapted after Hellwig et al. (2023). The time series was shortened to the vegetation phases (DOY 80–320). The dashed line indicates that data outside the valid period are used to calculate RWCVOD. This, combined with the use of the 5th and 95th percentiles, can theoretically result in physiologically invalid RWC_{VOD} values, which may be below 0% or above 100%. The figure was created with the same coloring as Figure 6.

Oliveira, 2019; McDowell et al., 2008). However, this reduces water-use efficiency at the expense of photosynthesis, leading to a decline in transpiration and, consequently, ET (Buras et al., 2020; Konings et al., 2021; Peters et al., 2018), as observed at the Hainich Forest.

Overall, this extreme water stress during the summer of 2018 severely affected the forest water status, which led to drought damage to beeches (Henkel et al., 2021; TMIL, 2022). During the summer, a two-month earlier and severe decline in vegetation greenness occurred (NDVI ~ 0.6) compared with 2017 (NDVI ~ 0.8, Figure 6f, orange arrow). At the same time, the vegetation water content declined more sharply than in the previous year (NDMI, Figure 6d, orange arrow). Both reflected the visual consequences of the drought damage, including completely desiccated tree canopies, severe leaf burning, and premature leaf discoloration at the end of July (TMIL, 2022). As a last emergency strategy, beech trees shed their green leaves to save water resources. Old-growth beech and ash trees (>60 years), making up a large share in Hainich, were particularly affected by this phenomenon, as they are less resistant to extreme drought conditions (TMIL, 2022). However, this depends on the location, temperature, and tree species. In general, warm and dry growing seasons that are less conducive to photosynthesis tend to delay the end of the growing season in the Hainich Forest (Kloos et al., 2024).

The extreme drought in the summer of 2018 also affected the drought-following years, 2019 and 2020, as the water stress persisted. Due to the absence of precipitation during the autumn of 2018 (Figure 5b), SM could not be refilled over the winter (SM_{-8cm} ~ 21 vol. % in November 2018 to ~35 vol. % in February 2019 compared to ~44 vol. % in 2017, Figure 6a). In 2019 and 2020, the deeper soil layers (25–200 cm depth) were impacted almost exclusively (Marx, 2022), also observed in the Hainich Forest (Figures S1b and S1c in Supporting Information S1). Although 2019 and 2020 were not as dry as 2018 or even near normal (Table S2 in Supporting

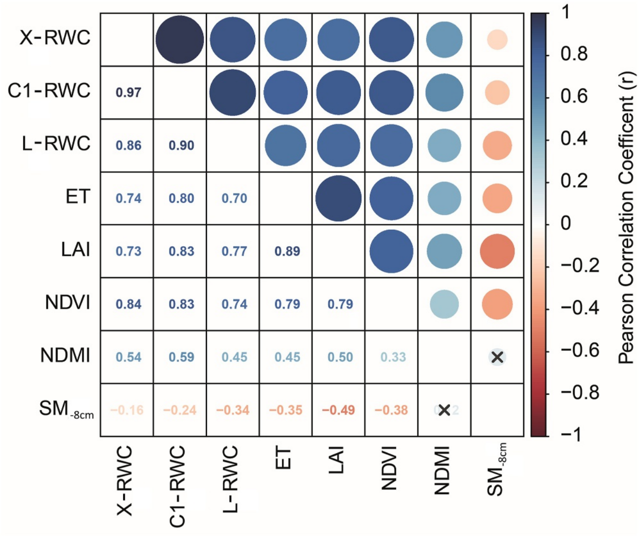

Figure 11. Pearson correlation coefficient (r) for the temporally aggregated AMSR2 X- and C1-band relative water content (RWC_{VOD}), SMAP DCA L-band RWC_{VOD}, in situ evapotranspiration (ET), leaf area index (LAI), normalized difference vegetation index (NDVI), normalized difference moisture index (NDMI), and in situ soil moisture from 8 cm soil depth (SM_{-8cm}) from the "DE-Hai" ICOS station for the vegetation period of 2015–2019. All values are significant to a p-value of 0.001. Exceptions are marked with ×.

Information S1), the lack of water led to further drought damage, such as scrawny twigs and branches as well as smaller leaf sizes (TMIL, 2022). In detail, the average crown thinning increased from 25.6% (2018) to 36.8% (2020), and the number of beech trees with more than 50% leaf loss almost quadrupled from 5.7% (2018) to 20.9% (2020) (TMIL, 2022). These general structural observations were also confirmed by Heidenreich and Seidel (2022), who found that overall structural complexity and branch length in the Hainich National Park most likely decreased due to droughts. Although 2021, after the 2018–2020 multi-year drought, was characterized by very high precipitation, one single year of abundant precipitation is not enough to compensate for the consequences of several consecutive drought years (Lee et al., 2023; Schellenberg et al., 2023; TMIL, 2022).

In addition to the water-related SPAS-based variables/proxies, optical remote sensing helps to identify most of these visual consequences of drought damage by detecting a decline in vegetation water content and vegetation greenness. However, microwave remote sensing data may be required to detect more reliably structural-related drought damages that became evident in the drought-following years (Section 5.2, Section 5.3).

5.2. Active Microwave Observations for Water Dynamics Monitoring

For the Hainich Forest, we observed moderate to high correlations between microwave remote sensing (i.e., RS-based variables) and SPAS-based variables/proxies (Figures 8 and 11). This suggests that SPAS-related water dynamics under different hydrological conditions can be tracked using multi-frequency active and passive microwave data. In general, for many of the following findings, appropriate filters were applied in addition to correlation and sensitivity analyses to gain further insights (Table 3, Table S1 in Supporting Information S1). These environmental and hydrological filters are universally applicable and transferable to other (forest) sites, as they are based on temperature and precipitation. Only the vegetation filters are tailored to a deciduous broadleaf site, allowing for the determination of leaf-on and leaf-off conditions. It is also important to note that third variables affect the relationship between S-1 backscatter and SPAS-based variables/proxies. For VPD, for example, this influence can be determined by using the hydrological filters (i.e., different atmospheric saturation states). Overall, we found the highest correlation between active microwave Sentinel-1 C-band SAR data (5.405 GHz) and water-related SPAS-based variables/proxies under more moist and dense vegetation conditions.

First, the correlation between S-1 $\gamma_{VH}^{evening}$ and SPAS-based variables/proxies is considerably higher under very wet conditions (2017, $|r| \sim 0.78$ on average) than under extremely dry conditions (2018, $|r| \sim 0.53$ on average) (Figure 9). As wet conditions are a key factor, selecting rewetting periods using the hydrological filter and removing snow and frost conditions further improves the correlation between S-1 $\gamma_{VH}^{evening}$ and SPAS-based variables/proxies, especially for the extremely dry year 2018 ($|\Delta r| \sim 0.08$ on average; Figure 9b). This indicates that, especially the snow and frost as well as the hydrological filters, applied on RS-based variables and SPAS-based variables/proxies are crucial in the context of drought-related analyses. To the best of our knowledge, this is the first study analyzing in detail the relationships of Sentinel-1 SAR data and SPAS-based variables/proxies under wet and dry conditions in beech forests. Nevertheless, several studies reported an increase in backscatter of ~0.7–~3 dB, especially at higher frequencies, due to intercepted rainfall in mixed and coniferous forests (Benninga et al., 2019; Dobson et al., 1991; M. El Hajj et al., 2016; Jong, 2000; Vaca & Van der Tol, 2018) but a decrease of 0–~2 dB in deciduous broadleaf forests (Dobson et al., 1991; Vaca & Van der Tol, 2018). This change in backscatter is most likely caused by the interception itself (Jong, 2000; Riedel et al., 2002), with the added weight on leaves changing their orientation, but it depends on the vegetation structure and the growth stage (Riedel et al., 2002) as well as on the amount and duration of the intercepted rain (Benninga et al., 2019). Furthermore, precipitation affects SPAS-based variables/proxies as the additional rainwater can recharge the soil water and increase plant transpiration due to the water cycle (Nobel, 2020; Tang et al., 2022; C. Wang et al., 2019). Both may explain the higher overall correlation between the Sentinel-1 backscatter and water-related SPAS-based variables/proxies under more moist and dense vegetation conditions.

Second, the Sentinel-1 backscatter is more sensitive to SPAS-based variables/proxies for evening acquisitions (~05:00 p.m. UTC): S-1 γ^{evening} shows higher correlations than S-1 γ^{morning} for the VH ($|\Delta r| \sim 0.13$ on average, not shown) and the VV polarization ($|\Delta r| \sim 0.19$ on average, not shown). The morning acquisitions (~05:30 a.m. UTC) were affected by dew, but several studies showed that the dew effect on SAR data is relatively small (Gillespie et al., 1990; Riedel et al., 2002) or negligible (Jackson & Moy, 1999), also for Sentinel-1 C-band (Benninga et al., 2019), as the drop size and dew deposits are relatively small compared to intercepted rainfall (Gillespie et al., 1990; Jackson & Moy, 1999; Riedel et al., 2002). In addition, Ghada et al. (2019) observed a bimodal precipitation diurnal cycle in Germany, characterized by a minor peak in the morning and a major peak in the afternoon, especially with south-westerly winds and higher precipitation amounts in summer (Ghada et al., 2019). Our analysis of the diurnal precipitation frequency at Hainich Forest (Figure S3 in Supporting Information S1) revealed a similar bimodal distribution with a higher precipitation probability in the afternoon. This indicates wetter conditions during the Sentinel-1 evening acquisition time (~05:00 p.m. UTC) and could explain the higher correlation to water-related SPAS-based variables/proxies.

Third, the correlation between S-1 γ^{evening} and water-related SPAS-based variables/proxies is considerably higher for the VH polarization ($|r| \sim 0.59$ on average) compared to the VV polarization ($|r| \sim 0.33$ on average, Figure 8). As multiple, randomly oriented scatterers in the canopy, such as leaves and twigs, lead to a depolarization of the transmitted electromagnetic waves, the VH polarization is more sensitive to vegetation volume scattering and would react more strongly to vegetation structure than the VV polarization, which is more sensitive to soil scattering and vertical structures (Freeman & Durden, 1998). Thus, several studies stated that the VH polarization appears more sensitive to the phenological cycle and the foliage dynamics in deciduous broadleaf forests than the VV polarization (Ling et al., 2022; Proietti et al., 2020; Rüetschi et al., 2019; Soudani et al., 2021), which is also consistent with our observation for the Hainich Forest. In addition, the water-based SPAS-based variables/proxies depend on the seasonal vegetation cycle (Nobel, 2020; C. Wang et al., 2019). A time lag analysis indicated that SPAS-based variables/proxies were interconnected ($|r| \sim 0.67$ on average; Figure 8) and temporally lagged, depending on environmental and hydrological conditions (Table S3 in Supporting Information S1). For instance, we observed that SM variations were lagged depending on the measurement depth: While S-1 $\gamma_{\text{VH}}^{\text{evening}}$ decreased in spring and increased in autumn, $\mathrm{SM}_{\text{-8cm}}$ follows directly or with a short delay (2017: 6d, 2018: 0d). This delay increases with increasing measurement depth ($\mathrm{SM}_{\text{-16cm}}$: 2017: 7d, 2018: 0d; $\mathrm{SM}_{\text{-32cm}}$: 2017: 15d, 2018: 9d). This could indicate a time lag in root water uptake (RWU) for different soil depths under wet conditions and, on the contrary, a more immediate RWU, also affecting deeper layers (e.g., $\mathrm{SM}_{\text{-16cm}}$) under drought conditions. However, it remains ambiguous if and how variations in the S-1 SAR signal are related to variations in SM through RWU. Nevertheless, since the SPAS-based variables/proxies depend on the phenological cycle and the VH polarization is particularly sensitive to the phenological cycle as well as moisture dynamics, this could explain the much higher correlation of S-1 $\gamma_{\text{VH}}^{\text{evening}}$ with water-related SPAS-based variables/proxies.

Fourth, an anti-cyclical (negative correlations) behavior between S-1 $\gamma_{\text{VH}}^{\text{evening}}$ and LAI, ET, and VPD could be observed (Figures 7a, 7c and 7d), indicating leaf-on and leaf-off conditions. This anti-cyclical behavior, that is, the decline of Sentinel-1 VH backscatter with the onset of the foliage (leaf-on conditions) and thus with increasing leaf biomass, has also been observed in other studies of deciduous broadleaf forests (Dostálová et al., 2018; Dubois et al., 2020; Frison et al., 2018; Ling et al., 2022; Soudani et al., 2021). In this context, it is crucial to understand that vegetation canopies can be sources (scattering) or sinks (absorption) of electromagnetic radiation depending on the biomass (foliage), water status, and dynamics along the seasons (Ulaby et al., 1986). This must be considered when analyzing and modeling electromagnetic interaction scenarios in tree canopies. Nevertheless, using the dense vegetation (mask) filter to consider only sparse vegetation periods (~October to ~April), we observed, first, a cyclical behavior with a positive correlation between S-1 $\gamma_{\text{VH}}^{\text{evening}}$ and ET ($r = 0.7$), and VPD ($r = 0.53$; Figure 9b) under no-frost, stable dry-down, and extremely dry conditions. This cyclical (reverse) behavior can be explained by the fact that under leaf-off conditions, the strong vegetation attenuation effect (i.e., anti-cyclical behavior: decreased VH backscatter due to increased leaf biomass) does not occur due to dense vegetation masking. In addition, this cyclic behavior has already been observed in less dense tree canopies, such as needleleaf trees, over the entire year (Jagdhuber et al., 2023; Mueller et al., 2022). Second, under these conditions (sparse vegetation, no-frost, stable dry-down, extremely dry), S-1 $\gamma_{\text{VH}}^{\text{evening}}$ and near soil surface $\mathrm{SM}_{\text{-8cm}}$ show the highest correlation ($r = 0.91$, Figure 9b), as dried-out canopies cause reduced microwave attenuation, allowing a deeper penetration of the C-band SAR signal into the canopy, leading to potentially more ground contribution (Ulaby et al., 1986). This indicates that S-1 $\gamma_{VH}^{evening}$ can track SM_{-8cm} under these conditions and thus report, in addition to vegetation-based, also water-based signs of drought.

Overall, our findings confirm that more moist and dense broadleaf canopies lead to increased microwave attenuation (i.e., reduced penetration depth), found in Hainich (Schellenberg et al., 2023; Zehner et al., 2023) and other deciduous broadleaf forest sites (Dostálová et al., 2018; Dubois et al., 2020; Frison et al., 2018; Ling et al., 2022; Soudani et al., 2021), most likely due to less reflection contribution from the ground and more absorption or forward-scattering of leaves, twigs, and smaller branches at C-band VH backscatter (Ahern et al., 1993; Dostálová et al., 2018; Frison et al., 2018; Ling et al., 2022). In addition, we observe that under leaf-on conditions (characterized by mostly negative correlations between SPAS-based variables/proxies and S-1 γ_{VH}), the anti-cyclical behavior prevails due to increased microwave attenuation and reduced S-1 γ_{VH} backscatter. Conversely, due to the absence of vegetation (leaf-off conditions), the behavior exhibits cyclic (positive correlations).

5.3. Passive Microwave Observations for Water Dynamics Monitoring

For the Hainich Forest, we found a high sensitivity of X- (10.65 GHz) and C-band (6.925 GHz) RWC_{VOD} to the water status of top canopy compartments, such as leaves and twigs, and of L-band (1.4 GHz) RWC_{VOD} to the water status of lower canopy compartments, such as branches and trunks. In addition, we observed that changes in water status can be captured more effectively with the use of multiple frequencies, that is, X-, C-, and L-band RWC_{VOD}.

First, our results are consistent with the expected sensing depth of different microwave frequencies (Ulaby et al., 1986). The sensitivity of X-band RWC_{VOD} to leaves is implied by the higher correlation to the NDVI ($r = 0.84$) than to the LAI ($r = 0.73$; Figure 11). The moderate to high correlation of C-band RWC_{VOD} with the mainly water-based NDMI ($r = 0.59$), compared to L-band RWC_{VOD} ($r = 0.45$, Figure 11), indicates sensitivity to the water status of top tree compartments, such as leaves and twigs. In contrast to the NDVI and NDMI, the LAI considers deeper vegetation layers, as it is based on a three-dimensional radiative transfer model, which accounts for different canopy levels (Knyazikhin et al., 1999). This aligns with the stronger relationship between LAI and L-band RWC_{VOD} ($r = 0.77$; Figure 11), indicating the sensitivity to the water status of lower tree compartments such as branches and trunks. These results are consistent with the theory, stating that lower frequencies interact with thicker objects due to their longer wavelengths and can therefore penetrate deeper into the canopy (Ulaby et al., 1986). Additionally, several remote sensing research papers confirm this in real-world examples (Chaparro et al., 2019; Li et al., 2021; Olivares-Cabello et al., 2023; Rodríguez-Fernández et al., 2018).

Second, X-, C-, and L-band RWC_{VOD} dynamics are similar over time despite the different frequencies and sensors used (Figures 10d–10f, $r \sim 0.91$ on average, Figure 11). This indicates that top and deeper tree compartments have comparable seasonal water content dynamics. Regarding these seasonal dynamics, during the spring reactivation phases, X-, C-, and L-band RWC_{VOD} rose due to the onset of vegetative growth. During this phase, the tree compartments become wetter, especially when the leaves rehydrate after dormancy (Nobel, 2020), also observed for broadleaf deciduous forests for the Advanced Scatterometer (ASCAT) C-band (Pfeil et al., 2020). In addition, X-, C-, and L-band RWC_{VOD} increased in parallel with NDVI and LAI at about DOY 80, where the canopy is not yet leafy (Figure S4 in Supporting Information S1). This is most likely due to RWC_{VOD} being sensitive to understorey development and plant water uptake (Chaparro et al., 2019; Holtzman et al., 2021).

Third, the vegetation indices peaked in June during the high foliage phase, which simultaneously implies high photosynthetic activity and water content of the leaf canopy (Figures 6e and 6f, Figure S4 in Supporting Information S1). This could also explain the first peak of X-, C-, and L-band RWC_{VOD}, as the respective sensitive tree compartments were particularly wet and active (Nobel, 2020). A similar behavior of VOD was also observed at other temperate broadleaf sites (Holtzman et al., 2021; Jones et al., 2011; Yao et al., 2024). In the following low foliage phase in July/August, the high TA, high radiation, and lower water reserves in summer led to the closure of the stomata of the leaves, leaf desiccation, and premature leaf shedding, and thus to a reduction in photosynthetic activity (Section 5.1, Figures 6a–6c; Buras et al., 2020; Konings et al., 2021; Peters et al., 2018). In addition, the understory also faded (Figure 2). These factors most likely led to a decrease in X-, C-, and L-band RWC_{VOD} in the low foliage phase after the first RWC_{VOD} peak (Figures 10d–10f), also observed for VOD at other temperate broadleaf sites (Holtzman et al., 2021; Yao et al., 2024). This decline was considerably greater at X-band RWC_{VOD} ($\sim -100\%$) for the drought year 2018 than for the very wet year 2017 ($\sim -70\%$; Figure 10d). The leading cause for

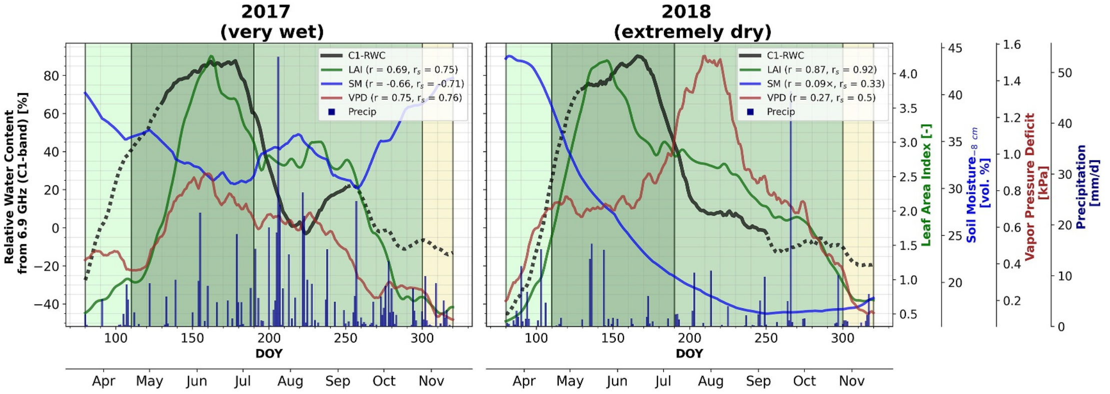

Figure 12. Time Series of relative water content ($\mathrm{RWC_{VOD}}$) derived from AMSR2 C1-band, leaf area index (LAI) utilized from MODIS, as well as daily in situ soil moisture (SM) from 8 cm soil depth, in situ vapor pressure deficit (VPD), and in situ precipitation amount in 2017 and 2018. The time series was shortened to the vegetation phases (DOY 80–320). r gives the Pearson and r_s the Spearman's rank correlation coefficient between the $\mathrm{RWC_{VOD}}$ and the variables, respectively, with all values being significant to a p-value of 0.001. Exceptions are marked with ×. The dashed line indicates that data outside the valid period are used to calculate $\mathrm{RWC_{VOD}}$. This, combined with the use of the 5th and 95th percentiles, can theoretically result in physiologically invalid $\mathrm{RWC_{VOD}}$ values, which may be below 0% or above 100%. The background was colored according to the respective vegetation phases (light green to yellow; Section 2.1, Figure 2).

this was that in 2018, the direct drought damages, such as entirely desiccated tree canopies and severe solar-induced leaf burning, were observed mainly in the very top canopy (TMIL, 2022). Due to the greater sensing depth, this $\mathrm{RWC_{VOD}}$ decay in 2018 is minor at C-band (Figure 6e) and probably no longer detectable at L-band (Figure 10f). In contrast, a smaller scattering effect during drought conditions compared to normal conditions can lead to increased L-VOD values (H. Wang et al., 2023) as also observed at the Hainich Forest (Figure 10f).

Fourth, a second $\mathrm{RWC_{VOD}}$ peak occurred under very wet conditions in September 2017 (Figures 10d–10f, 12). This peak was most likely vegetation- and water-related and was also influenced by a decreasing temperature and its effect on $\mathrm{RWC_{VOD}}$. Thus, the vegetation was saturated with water due to the unusually high precipitation amount in July (~182 mm, compared to ~22 mm in July 2018). Afterward, this water supply and the decreasing demand for water from the atmosphere ($\Delta\mathrm{VPD} = -0.13$ kPa) led to an increase in $\mathrm{SM_{\text{-}8cm}}$ ($\Delta = 0.05$ vol. %) and LAI ($\Delta = 0.4\ \mathrm{m^2 \times m^{-2}}$) a few days later at the beginning of August. Both effects most likely caused the rise of $\mathrm{RWC_{VOD}}$ from August 2017 onwards. This is also consistent with Harris et al. (2022), who found that strong wet intraseasonal events increase SM, PWU, and hence VOD, and can persist for 2 months, in less than a week after the rainfall peak, depending on land cover type. In contrast to 2017, the lack of precipitation (~18 mm), extremely high VPD (~1.5 kPa), and decreasing leaf area ($\Delta\mathrm{LAI} = -0.5\ \mathrm{m^2 \times m^{-2}}$) in August 2018 (Figures 5b, 6e and 7d) could have prevented a second peak of $\mathrm{RWC_{VOD}}$ in September 2018 (Figures 6e and 12) due to limited water supply (TMIL, 2022). Thus, C-band $\mathrm{RWC_{VOD}}$ was primarily vegetation-based in 2018 as indicated by its very high similarity to NDVI ($r = 0.95$, $r_s = 0.91$) and LAI ($r = 0.87$, $r_s = 0.92$; Figure 12).

However, still under very dry conditions, a second peak of $\mathrm{RWC_{VOD}}$ was observed in late summer 2019 for X- and C-band $\mathrm{RWC_{VOD}}$ (Figures 10d and 10e). This peak was most likely primarily related to changes in vegetation density. The sufficient amount of precipitation (~60 mm) and the moderately high VPD (~0.9 kPa) in August may have caused an increase in leaf area ($\Delta\mathrm{LAI} = 0.4\ \mathrm{m^2 \times m^{-2}}$) over the next few weeks (Figures 6e and 12). These effects could explain the rise of X- and C-band $\mathrm{RWC_{VOD}}$. Due to drought-related structural tree canopy damages from the previous extreme drought year (Heidenreich & Seidel, 2022; TMIL, 2022), the second peak of L-band $\mathrm{RWC_{VOD}}$ is more ambiguous and occurred a month earlier in mid-August 2019 (Figure 10).

The estimated $\mathrm{RWC_{VOD}}$ strongly depends on the assumption of effectively constant biomass conditions within the selected period for the RWC normalization. Since minor fluctuations in biomass within the selected period cannot be completely eliminated, the influence of biomass within $\mathrm{RWC_{VOD}}$ could still be present. The same applies to the temperature. In general, the effect of temperature on VOD variations is less compared to biomass, especially for L-band compared to X-band, and for seasonal compared to diurnal variations. Although this effect has been routinely neglected in regional and global VOD studies, its impact on VOD variations is larger than previously assumed (Zhao et al., 2024). In this study, within the selected period for normalization, $\mathrm{TA_{95}}$ is assumed to be effectively constant at 20°C (Figure 6c). However, isolated fluctuations of ~±5°C occur, as observed during August 2018. The impact of these temperature fluctuations on RWC_{VOD} has been quantified using a forward simulation of VOD based on Chaparro et al. (2024), parametrized with estimates and in situ information: an increase in TA_{95} ($\Delta TA_{95} = 5°C$, in relation to $TA_{95} = 20°C$) results in an increase in L-band RWC_{VOD} ($\Delta RWC_{VOD} \sim 10$–15%) and a decrease in X-band RWC_{VOD} ($\Delta RWC_{VOD} \sim -10\%$-15%). A decrease in TA_{95} ($\Delta TA_{95} = -5°C$, in relation to $TA_{95} = 20°C$) leads to exactly the opposite, which is consistent with the observations of Zhao et al. (2024). The estimated temperature-related overestimation or underestimation ($\Delta RWC_{VOD} \sim \pm 10$–15%) at selected points within the RWC_{VOD} time series does not affect our conclusions, as this study focuses more on the general seasonal patterns and the major features of RWC_{VOD} (i.e., RWC_{VOD} peaks and troughs, which are characterized by considerably stronger increases and decreases in RWC_{VOD} (±25–90%)) between wavelengths and years. Therefore, the proposed method for calculating RWC_{VOD} is also effective in the presence of limited temperature fluctuations. Its computation is straightforward, as it does not imply the use of semi-physical approaches or extensive in situ data, which facilitates its applicability and adoption for the analysis of water dynamics and vegetation droughts at seasonal scales. Thus, this makes RWC_{VOD} an efficient drought indicator. For future research, new semi-physical approaches to disentangle dry biomass, structure, and water content from VOD in forests could be applied, such as those described by Jagdhuber et al. (2022) or Chaparro et al. (2024). Furthermore, the effect of temperature on VOD should also be taken into consideration (Zhao et al., 2024).

Overall, L-band RWC_{VOD} seems to capture slower changes in water status in branches and trunks of lower tree compartments. The wet conditions in 2017 and spring 2018 resulted in a high amount of water stored in woody tissues, which were initially not particularly affected despite the onset of the drought in summer 2018 (Dou et al., 2024; TMIL, 2022). However, due to a moisture legacy effect, the actual drought damage will only become visible in the drought-following years (Bastos et al., 2020; Buras et al., 2020; Dou et al., 2024; Kannenberg et al., 2019; Schellenberg et al., 2023; Thonfeld et al., 2022). In particular, the extreme drought conditions in 2018 decreased the overall structural complexity of the beech canopies and the vitality of beeches in the drought-following years (Heidenreich & Seidel, 2022; TMIL, 2022). As L-band RWC_{VOD} was considerably reduced during the high foliage phase in the drought-following year 2019 (Figure 10f), this indicates that L-band can detect the legacy effects from the previous extreme drought in 2018, which is also consistent with prior research (Frappart et al., 2020; Olivares-Cabello et al., 2023). Therefore, L-band RWC_{VOD} data can capture legacy effects from past drought conditions, as the recovery of the woody component is slower than that of the leaf component (Dou et al., 2024), and multi-year droughts. In contrast, RWC_{VOD} at higher frequencies (X- and C-band) can detect fast water content changes in leaves and twigs of the top canopy, rapidly responding to the drought onset in summer 2018. This is because X- and C-band RWC_{VOD} are sensitive to leaf tissues, whose water content may be closely linked to changes in environmental conditions. Since this water content was reduced more and earlier under drought conditions, remotely sensed X- and C-band RWC_{VOD} data are valuable indicators for identifying the beginning of droughts.

6. Conclusions

In this study, we compared time series of active and passive microwave as well as optical remote sensing with multiple components of the soil-plant-atmosphere system (SPAS) in a temperate forest. By using SPAS-based variables/proxies, we assessed the water status and dynamics over 6 years, encompassing both drought and non-drought conditions. The study period was characterized by the exceptional 2018–2020 multi-year drought, setting a new benchmark record for all droughts since 1766 in Europe (Bastos et al., 2020; Buras et al., 2020; Marx, 2022; Rakovec et al., 2022). This multi-year drought affected over one-third of all Thuringian beeches (TMIL, 2022). Our data show that 2017 was exposed to much rain, which resulted in earlier and stronger vegetation growth in the spring of 2018. Consequently, evapotranspiration increased earlier, and soil moisture (SM) was depleted faster, leading to an exacerbation of the drought during the summer (Bastos et al., 2020), which is also confirmed by our data. In addition, the shallow main root area in the protected beech and near-natural mixed Hainich Forest, combined with very dry atmospheric conditions and prolonged dry-down phases, caused extreme water stress. This resulted in severe drought damages, such as fully desiccated tree canopies, severe leaf burning, and premature leaf shedding in the summer of 2018 and over the drought-following years, 2019 and 2020, as the water stress persisted (TMIL, 2022), which is also reflected in our used SPAS-based variables/proxies. Furthermore, the future droughts predicted for Europe will be of comparable intensity to the multi-year drought 2018–2020, but will last significantly longer than any drought observed (Rakovec et al., 2022). Since the European beech generally cannot tolerate prolonged dry periods and extreme heat, this could lead to a future reduction in growth and possible retreat of drought-prone beech forests, copying similar patterns already found in Southern Europe ∼20 years ago (Jump et al., 2006).

We focused on the investigation of Sentinel-1 C-band VV and VH-polarized backscatter (S-1 γ^0; 5.405 GHz) and the relative water content estimated from vegetation optical depth (RWC$_{\text{VOD}}$) of AMSR2 (X- and C-band; 10.65 and 6.925 GHz) and SMAP (L-band; 1.4 GHz). For active microwaves, we found the highest sensitivity between S-1 γ^0 and water-related SPAS-based variables/proxies for the VH polarization and evening acquisitions (S-1 $\gamma_{\text{VH}}^{\text{evening}}$). On the one hand, S-1 $\gamma_{\text{VH}}^{\text{evening}}$ can track near soil surface SM$_{\text{-8cm}}$ ($r = 0.91$) under sparse vegetation (leaf-off, approximately October to April), no-frost, stable dry-down, and extremely dry conditions (2018) in a deciduous broadleaf forest. This also highlights the importance of hydrological filters in the context of drought-related analyses. On the other hand, S-1 $\gamma_{\text{VH}}^{\text{evening}}$ is most influenced by the leaf area index (LAI; $r = -0.94$) under dense vegetation (leaf-on), no-frost, and very wet conditions (2017). Both are consistent with the observation that more moist and dense broadleaf canopies lead to increased microwave attenuation (i.e., reduced penetration depth), found in the Hainich Forest (Schellenberg et al., 2023; Zehner et al., 2023) and other deciduous broadleaf forest sites (Dostálová et al., 2018; Dubois et al., 2020; Frison et al., 2018; Ling et al., 2022; Proietti et al., 2020; Soudani et al., 2021). We follow the hypothesis that less reflection contribution from the ground and more absorption or forward-scattering of leaves, twigs, and smaller branches might cause this increased microwave attenuation at C-band VH polarization, and thus, reduced S-1 γ_{VH} backscatter (Ahern et al., 1993; Dostálová et al., 2018; Frison et al., 2018; Ling et al., 2022). We conclude that the anti-cyclical behavior (characterized by mostly negative correlations between SPAS-based variables/proxies and S-1 γ_{VH}) predominates under leaf-on conditions due to the increased microwave attenuation and reduced S-1 γ_{VH} backscatter. On the contrary, this behavior exhibits cyclic (positive correlations) for phases with an absence of vegetation (leaf-off conditions).

For multi-frequency passive microwaves, we found that X- and C-band RWC$_{\text{VOD}}$ can capture foliage-related drought damages in the very top of the canopy by identifying fast water content changes in leaves and twigs due to their sensitivity to leaf tissues and shallow sensing depth. Therefore, remotely sensed X- and C-band RWC$_{\text{VOD}}$ data are valuable indicators for detecting the onset of droughts. On the contrary, L-band RWC$_{\text{VOD}}$ can identify slower changes in water status in branches and trunks of lower tree compartments by capturing the structural-related drought damages, which are linked to woody tissues, consistent with previous research (Frappart et al., 2020; Olivares-Cabello et al., 2023). These damages became apparent in the drought-following years due to a moisture legacy effect (Bastos et al., 2020; Buras et al., 2020; Dou et al., 2024; Heidenreich & Seidel, 2022; Kannenberg et al., 2019; Schellenberg et al., 2023; Thonfeld et al., 2022; TMIL, 2022), as the recovery of the woody component is slower than that of the leaf component (Dou et al., 2024). Therefore, our results indicate that remotely sensed L-band RWC$_{\text{VOD}}$ data are suitable for detecting legacy effects from past drought conditions and multi-year droughts.

Overall, we found that water-related SPAS-based variables/proxies can be successfully tracked using remotely sensed active and passive microwave and optical time series, along with appropriate filtering and selection procedures. We demonstrated that the water status and dynamics of a deciduous broadleaf forest can be captured under both drought and non-drought conditions. Different vertical forest canopy layers can be accessed using multiple frequencies as well as active and passive sensing technologies. As further analyses, using in situ gravimetric water content of vegetation (m_g) information, RWC$_{\text{VOD}}$ could be linked to the minimum and maximum m_g values. Afterward, by applying pressure-volume curves, from water storage information, water potential (e.g., forest water potential (Jagdhuber et al., 2025), and finally water fluxes (e.g., plant water uptake or transpiration rate (Jagdhuber et al., 2022) could be estimated. For future forest monitoring, the upcoming Copernicus Imaging Microwave Radiometer (CIMR) mission, which will carry Ka-, K-, X-, C-, and L-band passive sensors on a single instrument, is of particular importance (Donlon et al., 2026). On the one hand, the CIMR mission will enhance multi-frequency VOD retrievals, as Ka-to L-band observations will be available simultaneously from the same instrument. Thus, fewer ancillary data will be required (i.e., the use of canopy temperature from CIMR's Ka-band). On the other hand, the temporal mismatch will be removed, allowing simultaneous access to the different vertical canopy layers (i.e., from leaf to trunk level). Other promising upcoming or recently launched SAR missions are NASA-ISRO Synthetic Aperture Radar (NISAR; S- and L-band; Kellogg et al., 2020), Radar Observation System for Europe L-band SAR (ROSE-L; L-band; Petrolati et al., 2023), and BIOMASS (P-band; Gelas et al., 2021).

Altogether, two factors are essential for future continuous SPAS monitoring. On the one hand, this includes continuation of novel satellite missions (e.g., CIMR, NISAR, ROSE-L, BIOMASS) and high spatio-temporal follow-on missions such as Sentinel-1C (Torres et al., 2022). On the other hand, the expansion of standardized monitoring in situ networks at forest sites, such as the Integrated Carbon Observation System (ICOS; ICOS RI, 2024), and more frequent forest inventories are crucial. First, the SPAS can already be assessed based on these in situ data alone, as demonstrated in this study. Second, in situ data enable ground truthing and thus verified remote sensing and spatio-temporal forest monitoring on a large scale.

We conclude that using multi-year and multi-frequency active and passive microwave and optical remote sensing data jointly is crucial for monitoring different vertical tree compartments. These data enable us to assess not only the water status but also the water dynamics of tissues and ultimately the ecohydrological resilience of forest canopies. Thus, remote sensing, combined with in situ data, is key for comprehensive SPAS-based climate monitoring at larger spatio-temporal scales.

Conflict of Interest

The authors declare no conflicts of interest relevant to this study.

Availability Statement

The ICOS data set is available at https://doi.org/10.18160/CR66-PJ24, last access: 13 November 2023 (Knohl et al., 2022). DWD data are available at https://opendata.dwd.de/climate_environment/CDC/observations_germany/, last access: 17 November 2023 (DWD, 2021). The AMSR2/GCOM-W1 surface soil moisture (LPRM) and VOD data set is available at https://doi.org/10.5067/B0GHODHJLDA8, last access: 14 November 2023 (Jeu & Owe, 2014; Owe et al., 2008). The SMAP DCA (SPL3SMP_E) VOD data set is available at https://doi.org/10.5067/NJ34TQ2LFE90, last access: 14 November 2023 (O'Neill, Chan, et al., 2020). The MODIS LAI (MCD15A3H) data set is available at https://doi.org/10.5067/MODIS/MCD15A3H.061, last access: 26 May 2024 (Myneni et al., 2021). The MODIS Surface Reflectance (MCD19A1) data set is available at https://doi.org/10.5067/MODIS/MCD19A1.061, last access: 15 November 2023 (Lyapustin & Wang, 2022). The Corine Land Cover 2018 data set is available at https://doi.org/10.2909/960998c1-1870-4e82-8051-6485205ebbac, last access: 15 November 2023 (EAA, 2019). The Tree Cover Density 2018 data set is available at https://doi.org/10.2909/c7bf34ea-755c-4dbd-85b6-4efc5fd302a2, last access: 15 November 2023 (EAA, 2020).

Acknowledgments

F. Hellwig is funded by the Deutsche Forschungsgemeinschaft (DFG, German Research Foundation)—514721519 in the project "Remote sensing of vegetation canopy properties: States and spatio-temporal dynamics‘ as part of the DFG Research Unit 5639: Land Atmosphere Feedback Initiative (LAFI). D. Chaparro has been funded by the projects "la Caixa" Junior Leader Fellowship LCF/BQ/PI25/12100008 (lead: D. Chaparro) and LCF/BQ/PI23/11970013 (lead: O. Binks) and by the project H2020 FORGENIUS (Improving access to FORest GENetic resources Information and services for end-USers) #862221. M. Piles has been supported by the waterMINT project (PID2024-160289OB-I00) funded by MICIU/AEI, Spain/FEDER, UE. The Bioclimatology group of the University of Göttingen acknowledges support by the German Federal Ministry of Education and Research (BMBF) as part of the European Integrated Carbon Observation System (ICOS) by the Deutsche Forschungsgemeinschaft (INST 186/1118-1 FUGG). We would like to thank Prof. Dr. Dara Entekhabi from the Massachusetts Institute of Technology (MIT) (Department of Civil and Environmental Engineering, Cambridge, USA) for his support and advice during this study. We would also like to thank all groups of predecessors and technical staff from the Bioclimatology Group of the University of Göttingen and the Max Planck Institute for Biogeochemistry for establishing the study site, for their continuous support in data acquisition and instrument maintenance, as well as the administration of the Hainich National Park for the opportunity to conduct research within the National Park. Open Access funding enabled and organized by Projekt DEAL.

References

Ahern, F. J., Leckie, D. J., & Drieman, J. A. (1993). Seasonal changes in relative C-band backscatter of northern forest cover types. *IEEE Transactions on Geoscience and Remote Sensing*, *31*(3), 668–680. https://doi.org/10.1109/36.225533

Allen, R. G., Pereira, L. S., Raes, D., & Smith, M. (1998). Crop evapotranspiration - Guidelines for computing crop water requirements: FAO irrigation and drainage paper 56. *Food and Agriculture Organization of the United Nations*. https://appgeodb.nancy.inra.fr/biljou/pdf/Allen_FAO1998.pdf

Anthoni, P. M., Knohl, A., Rebmann, C., Freibauer, A., Mund, M., Ziegler, W., et al. (2004). Forest and agricultural land-use-dependent CO_2 exchange in Thuringia, Germany. *Global Change Biology*, *10*(12), 2005–2019. https://doi.org/10.1111/j.1365-2486.2004.00863.x

Bastos, A., Ciais, P., Friedlingstein, P., Sitch, S., Pongratz, J., Fan, L., et al. (2020). Direct and seasonal legacy effects of the 2018 heat wave and drought on European ecosystem productivity. *Science Advances*, *6*(24), eaba2724. https://doi.org/10.1126/sciadv.aba2724

Bauer-Marschallinger, B., Freeman, V., Cao, S., Paulik, C., Schaufler, S., Stachl, T., et al. (2019). Toward global soil moisture monitoring with Sentinel-1: Harnessing assets and overcoming obstacles. *IEEE Transactions on Geoscience and Remote Sensing*, *57*(1), 520–539. https://doi.org/10.1109/TGRS.2018.2858004

Beer, C., Reichstein, M., Tomelleri, E., Ciais, P., Jung, M., Carvalhais, N., et al. (2010). Terrestrial gross carbon dioxide uptake: Global distribution and covariation with climate. *Science (New York, N.Y.)*, *329*(5993), 834–838. https://doi.org/10.1126/science.1184984

Bender, S., & Schaller, M. (2012). Vergleichendes Lexikon: Wichtige Definitionen, Schwellenwerte, Kenndaten und Indices für Fragestellungen rund um das Thema "Klimawandel und seine Folge". Retrieved from https://www.climate-service-center.de/imperia/md/content/csc/lexikon_definitionen_mit_cover.pdf

Benninga, H.-J., Van der Velde, R., & Su, Z. (2019). Impacts of radiometric uncertainty and weather-related surface conditions on soil moisture retrievals with Sentinel-1. *Remote Sensing*, *11*(17), 2025. https://doi.org/10.3390/rs11172025

Brockwell, P. J., & Davis, R. A. (2016). In *Introduction to time series and forecasting (Third edition)*. Springer texts in statistics. Springer. https://doi.org/10.1007/978-3-319-29854-2

Buras, A., Rammig, A., & Zang, C. S. (2020). Quantifying impacts of the 2018 drought on European ecosystems in comparison to 2003. *Biogeosciences*, *17*(6), 1655–1672. https://doi.org/10.5194/bg-17-1655-2020

Chaparro, D., Duveiller, G., Piles, M., Cescatti, A., Vall-llossera, M., Camps, A., & Entekhabi, D. (2019). Sensitivity of L-band vegetation optical depth to carbon stocks in tropical forests: A comparison to higher frequencies and optical indices. *Remote Sensing of Environment*, *232*, 111303. https://doi.org/10.1016/j.rse.2019.111303

Chaparro, D., Jagdhuber, T., Piles, M., Entekhabi, D., Jonard, F., Fluhrer, A., et al. (2021). Global L-Band vegetation volume fraction estimates for modeling vegetation optical depth. In *2021 IEEE International geoscience and remote sensing symposium IGARSS* (pp. 6399–6402). IEEE. https://doi.org/10.1109/IGARSS47720.2021.9554872

Chaparro, D., Jagdhuber, T., Piles, M., Jonard, F., Fluhrer, A., Vall-llossera, M., et al. (2024). Vegetation moisture estimation in the Western United States using radiometer-radar-lidar synergy. *Remote Sensing of Environment*, *303*, 113993. https://doi.org/10.1016/j.rse.2024.113993

Chaubell, M. J., Chan, S., Dunbar, R. S., Entekhabi, D., Peng, J., Piepmeier, J., & Yueh, S. (2017). Backus-gilbert optimal interpoaltion applied to enhance SMAP data: Implementation and assessment. In *2017 IEEE international geoscience and remote sensing symposium (IGARSS)* (pp. 2531–2534). IEEE. https://doi.org/10.1109/IGARSS.2017.8127510

Chaubell, M. J., Yueh, S. H., Dunbar, R. S., Colliander, A., Chen, F., Chan, S. K., et al. (2020). Improved SMAP dual-channel Algorithm for the retrieval of soil moisture. *IEEE Transactions on Geoscience and Remote Sensing*, *58*(6), 3894–3905. https://doi.org/10.1109/TGRS.2019.2959239

Das, N., Entekhabi, D., Kim, S., Yueh, S., Dunbar, R., & Colliander, A. (2017). SMAP/Sentinel-1 L2 radiometer/radar 30-Second scene 3 km EASE-grid soil moisture, version 1. https://doi.org/10.5067/9UWR1WTHW1WN

Dobson, M. C., Pierce, L., McDonald, K., & Sharik, T. (1991). Seasonal change in radar backscatter from mixed conifer and hardwood frorests in northern Michigan. In *[proceedings] IGARSS'91 remote sensing: Global monitoring for Earth management* (pp. 1121–1124). IEEE. https://doi.org/10.1109/IGARSS.1991.579268

Donlon, et al. (2026). CIMR mission requirements document v6.0. Retrieved from https://esamultimedia.esa.int/docs/EarthObservation/CIMR-MRD-v6.0-20260324-ISSUED.pdf

Dostálová, A., Wagner, W., Milenković, M., & Hollaus, M. (2018). Annual seasonality in Sentinel-1 signal for forest mapping and forest type classification. *International Journal of Remote Sensing*, *39*(21), 7738–7760. https://doi.org/10.1080/01431161.2018.1479788

Dou, Y., Tian, F., Wigneron, J.-P., Li, X. [X.], Zhang, W., Chen, Y., et al. (2024). Satellite observations indicate slower recovery of woody components compared to upper-canopy and leaves in tropical rainforests after drought. *Communications Earth and Environment*, *5*(1), 725. https://doi.org/10.1038/s43247-024-01892-9

Dubois, C., Mueller, M. M., Pathe, C., Jagdhuber, T., Cremer, F., Thiel, C., & Schmullius, C. (2020). Characterization of land cover seasonality in Sentinel-1 time series data. *ISPRS Annals of the Photogrammetry, Remote Sensing and Spatial Information Sciences*, *V-3–2020*, 97–104. https://doi.org/10.5194/isprs-annals-V-3-2020-97-2020

DWD. (2019). Jahrbuch 2018 des Deutschen Wetterdienstes. Retrieved from https://www.dwd.de/DE/leistungen/jahresberichte_dwd/jahresberichte_pdf/jahresbericht_2018.pdf;jsessionid=315FDABBC83A3AC9083BD39703A5D70A.live31084?__blob=publicationFile&v=7

DWD. (2021). Opendata. Mühlhausen/Thüringen-Görmar [Dataset]. *Deutscher Wetterdienst*. Retrieved from https://opendata.dwd.de/climate_environment/CDC/observations_germany/

EAA. (2019). Corine land cover 2018 (raster 100 m), Europe, 6-yearly - Version 2020_20u1, May 2020 [Dataset]. *European Environment Agency*. https://doi.org/10.2909/960998c1-1870-4e82-8051-6485205ebba

EAA. (2020). Tree cover density 2018 (raster 100 m), Europe, 3-yearly, September 2020 [Dataset]. *European Environment Agency*. https://doi.org/10.2909/c7bf34ea-755c-4dbd-85b6-4efc5fd302a2

El Hajj, M., Baghdadi, N., Zribi, M., & Angelliaume, S. (2016). Analysis of Sentinel-1 radiometric stability and quality for land surface applications. *Remote Sensing*, *8*(5), 406. https://doi.org/10.3390/rs8050406

El Hajj, M. M., Johansen, K., Almashharawi, S. K., & McCabe, M. F. (2023). Water uptake rates over olive orchards using Sentinel-1 synthetic aperture radar data. *Agricultural Water Management*, *288*, 108462. https://doi.org/10.1016/j.agwat.2023.108462

Feldman, A. F., Short Gianotti, D. J., Dong, J., Akbar, R., Crow, W. T., McColl, K. A., et al. (2023). Remotely sensed soil moisture can capture dynamics relevant to plant water uptake. *Water Resources Research*, *59*(2), e2022WR033814. Article. https://doi.org/10.1029/2022WR033814

Feldman, A. F., Short Gianotti, D. J., Konings, A. G., McColl, K. A., Akbar, R., Salvucci, G. D., & Entekhabi, D. (2018). Moisture pulse-reserve in the soil-plant continuum observed across biomes. *Nature Plants*, *4*(12), 1026–1033. https://doi.org/10.1038/s41477-018-0304-9

Fink, A., Jagdhuber, T., Piles, M., Grant, J., Baur, M., Link, M., & Entekhabi, D. (2018). Estimating gravimetric moisture of vegetation using an attenuation-based multi-sensor approach. In *2018 IEEE international geoscience and remote sensing symposium IGARSS* (pp. 353–356). IEEE. https://doi.org/10.1109/IGARSS.2018.8518949

Forkel, M., Schmidt, L., Zotta, R.-M., Dorigo, W., & Yebra, M. (2023). Estimating leaf moisture content at global scale from passive microwave satellite observations of vegetation optical depth. *Hydrology and Earth System Sciences*, *27*(1), 39–68. https://doi.org/10.5194/hess-27-39-2023

Foucras, M., Zribi, M., Albergel, C., Baghdadi, N., Calvet, J.-C., & Pellarin, T. (2020). Estimating 500-m resolution soil moisture using Sentinel-1 and optical data synergy. *Water*, *12*(3), 866. https://doi.org/10.3390/w12030866

Frappart, F., Wigneron, J.-P., Li, X. [X.], Liu, X., Al-Yaari, A., Fan, L., et al. (2020). Global monitoring of the vegetation dynamics from the vegetation optical depth (VOD): A review. *Remote Sensing*, *12*(18), 2915. https://doi.org/10.3390/rs12182915

Freeman, A., & Durden, S. L. (1998). A three-component scattering model for polarimetric SAR data. *IEEE Transactions on Geoscience and Remote Sensing*, *36*(3), 963–973. https://doi.org/10.1109/36.673687

Frison, P.-L., Fruneau, B., Kmiha, S., Soudani, K., Dufrêne, E., Le Toan, T., et al. (2018). Potential of Sentinel-1 data for monitoring temperate mixed forest phenology. *Remote Sensing*, *10*(12), 2049. https://doi.org/10.3390/rs10122049

Gao, Q., Zribi, M., Escorihuela, M. J., & Baghdadi, N. (2017). Synergetic use of Sentinel-1 and Sentinel-2 data for soil moisture Mapping at 100 m resolution. *Sensors*, *17*(9), 1966. https://doi.org/10.3390/s17091966

Gardner, W. R. (1960). Dynamic aspects of water availability to plants. *Soil Science*, *89*(2), 63–73. https://doi.org/10.1097/00010694-196002000-00001

Gardner, W. R. (1965). Dynamic aspects of soil-water availability to plants. *Annual Review of Plant Physiology*, *16*(1), 323–342. https://doi.org/10.1146/annurev.pp.16.060165.001543

Gelas, C., Villard, L., Ferro-Famil, L., Polidori, L., Koleck, T., & Daniel, S. (2021). Multi-Temporal speckle filtering of polarimetric P-Band SAR data over dense tropical forests: Study case in French Guiana for the BIOMASS mission. *Remote Sensing*, *13*(1), 142. https://doi.org/10.3390/rs13010142

Gentine, P., Green, J. K., Guérin, M., Humphrey, V., Seneviratne, S. I., Zhang, Y., & Zhou, S. (2019). Coupling between the terrestrial carbon and water Cycles—A review. *Environmental Research Letters*, *14*(8), 83003. https://doi.org/10.1088/1748-9326/ab22d6

Ghada, W., Yuan, Y., Wastl, C., Estrella, N., & Menzel, A. (2019). Precipitation diurnal cycle in Germany linked to large-scale weather circulations. *Atmosphere*, *10*(9), 545. https://doi.org/10.3390/atmos10090545

Gharun, M., Shekhar, A., Xiao, J., Li, X. [X.], & Buchmann, N. (2024). Effect of the 2022 summer drought across forest types in Europe. *Biogeosciences*, *21*(23), 5481–5494. https://doi.org/10.5194/bg-21-5481-2024

Giardina, F., Gentine, P., Konings, A. G., Seneviratne, S. I., & Stocker, B. D. (2023). Diagnosing evapotranspiration responses to water deficit across biomes using deep learning. *New Phytologist*, *240*(3), 968–983. https://doi.org/10.1111/nph.19197

Gillespie, T. J., Brisco, B., Brown, R. J., & Sofko, G. J. (1990). Radar detection of a dew event in wheat. *Remote Sensing of Environment*, *33*(3), 151–156. https://doi.org/10.1016/0034-4257(90)90026-I

Hammond, W. M., Williams, A. P., Abatzoglou, J. T., Adams, H. D., Klein, T., López, R., et al. (2022). Global field observations of tree die-off reveal hotter-drought fingerprint for earth's forests. *Nature Communications*, *13*(1), 1761. https://doi.org/10.1038/s41467-022-29289-2

Harris, B. L., Taylor, C. M., Weedon, G. P., Talib, J., Dorigo, W., & Van der Schalie, R. (2022). Satellite-observed vegetation responses to intraseasonal precipitation variability. *Geophysical Research Letters*, *49*(15), e2022GL099635. https://doi.org/10.1029/2022GL099635

Heidenreich, M. G., & Seidel, D. (2022). Assessing forest vitality and forest structure using 3D data: A case study from the hainich national park, Germany. *Frontiers in Forests and Global Change*, *5*, 929106. https://doi.org/10.3389/ffgc.2022.929106

Hellwig, F. M., Jagdhuber, T., Fluhrer, A., Dubois, C., Chaparro, D., Schellenberg, K., et al. (2023). Multi-frequency radiometry for multi-year monitoring of relative water content in A temperate forest. In *2023 IEEE international geoscience and remote sensing symposium IGARSS*. IEEE. https://doi.org/10.1109/IGARSS52108.2023.10281760

Henkel, A., Hese, S., & Thiel, C. (2021). Erhöhte Buchenmortalität im Nationalpark Hainich? *AFZ/Der Wald*, *2022*(3), 26–29. https://www.researchgate.net/profile/Soeren-Hese/publication/356665367_Erhohte_Buchenmortalitat_im_Nationalpark_Hainich/links/62137a7c6c472329dcfaf783/Erhoehte-Buchenmortalitaet-im-Nationalpark-Hainich.pdf

Holtzman, N. M., Anderegg, L. D. L., Kraatz, S., Mavrovic, A., Sonnentag, O., Pappas, C., et al. (2021). L-band vegetation optical depth as an indicator of plant water potential in a temperate deciduous forest stand. *Biogeosciences*, *18*(2), 739–753. https://doi.org/10.5194/bg-18-739-2021

ICOS RI (2024). *ICOS handbook 2024*. ICOS ERIC. https://doi.org/10.18160/28AV-80QR

Jackson, T. J., & Moy, L. (1999). Dew effects on passive microwave observations of land surfaces. *Remote Sensing of Environment*, *70*(2), 129–137. https://doi.org/10.1016/S0034-4257(99)00021-8

Jackson, T. J., & Schmugge, T. J. (1991). Vegetation effects on the microwave emission of soils. *Remote Sensing of Environment*, *36*(3), 203–212. https://doi.org/10.1016/0034-4257(91)90057-D

Jagdhuber, T., Fluhrer, A., Chaparro, D., Dubois, C., Hellwig, F. M., Bayat, B., et al. (2023). On the potential of active and passive microwave remote sensing for tracking seasonal dynamics of evapotranspiration. In *2023 IEEE international geoscience and remote sensing symposium IGARSS*. IEEE. https://doi.org/10.1109/IGARSS52108.2023.10283234

Jagdhuber, T., Jonard, F., Fluhrer, A., Chaparro, D., Baur, M. J., Meyer, T., & Piles, M. (2022). Toward estimation of seasonal water dynamics of winter wheat from ground-based L-band radiometry: A concept study. *Biogeosciences*, *19*(8), 2273–2294. https://doi.org/10.5194/bg-19-2273-2022

Jagdhuber, T., Schmidt, A.-S., Fluhrer, A., Chaparro, D., Jonard, F., Piles, M., et al. (2025). Estimation of forest water potential from ground-based L-Band radiometry. *IEEE Journal of Selected Topics in Applied Earth Observations and Remote Sensing*, *18*, 5509–5522. https://doi.org/10.1109/JSTARS.2025.3533567

Jeu, R. d., & Owe, M. (2014). AMSR2/GCOM-W1 surface soil moisture (LPRM) L3 1 day 10 km x 10 km ascending, V001 [Dataset]. https://doi.org/10.5067/B0GHODHJLDA8

Jones, M. O., Jones, L. A., Kimball, J. S., & McDonald, K. C. (2011). Satellite passive microwave remote sensing for monitoring global land surface phenology. *Remote Sensing of Environment*, *115*(4), 1102–1114. https://doi.org/10.1016/j.rse.2010.12.015

Jong, J. d. (2000). Rain storage in forests detected with ERS Tandem mission SAR. *Remote Sensing of Environment*, *72*(2), 170–180. https://doi.org/10.1016/S0034-4257(99)00100-5

Jump, A., Hunt, J. M., & Penuelas, J. (2006). Rapid climate change-related growth decline at the southern range edge of Fagus sylvatica. *Global Change Biology*, *12*(11), 2163–2174. https://doi.org/10.1111/j.1365-2486.2006.01250.x

Kannenberg, S. A., Maxwell, J. T., Pederson, N., D'Orangeville, L., Ficklin, D. L., & Phillips, R. P. (2019). Drought legacies are dependent on water table depth, wood anatomy and drought timing across the eastern US. *Ecology Letters*, *22*(1), 119–127. https://doi.org/10.1111/ele.13173

Kellogg, K., Hoffman, P., Standley, S., Shaffer, S., Rosen, P., Edelstein, W., et al. (2020). NASA-ISRO synthetic aperture radar (NISAR) mission. In *2020 IEEE aerospace conference* (pp. 1–21). IEEE. https://doi.org/10.1109/AERO47225.2020.9172638

Kloos, S., Klosterhalfen, A., Knohl, A., & Menzel, A. (2024). Decoding autumn phenology: Unraveling the link between observation methods and detected environmental cues. *Global Change Biology*, *30*(3), e17231. https://doi.org/10.1111/gcb.17231

Klosterhalfen, A., Fellert, D., Koebsch, F., Kreilein, H., Markwitz, C., Mund, M., et al. (2023). Analysis of a 23-years long eddy-covariance fluxes dataset from a mixed deciduous forest in Germany. https://doi.org/10.5194/egusphere-egu23-13689

Knohl, A., Siebicke, L., Tiedemann, F., & Kolle, O., & ICOS Ecosystem Thematic Centre. (2022). Warm winter 2020 ecosystem eddy covariance flux product from Hainich, Version 1.0 [Dataset]. https://doi.org/10.18160/CR66-PJ24

Knyazikhin, Y., Glassy, J., Privette, J., Tian, Y., Lotsch, A., Zhang, Y., et al. (1999). MODIS leaf area index (LAI) and fraction of photosynthetically active radiation absorbed by vegetation (FPAR) product (MOD15) algorithm theoretical basis document. Retrieved from http://eospso.gsfc.nasa.gov/atbd/modistables.html

Konings, A. G., Rao, K., & Steele-Dunne, S. C. (2019). Macro to micro: Microwave remote sensing of plant water content for physiology and ecology. *New Phytologist*, *223*(3), 1166–1172. https://doi.org/10.1111/nph.15808

Konings, A. G., Saatchi, S. S., Frankenberg, C., Keller, M., Leshyk, V., Anderegg, W. R. L., et al. (2021). Detecting forest response to droughts with global observations of vegetation water content. *Global Change Biology*, *27*(23), 6005–6024. https://doi.org/10.1111/gcb.15872

Lambers, H., & Oliveira, R. S. (2019). *Plant physiological ecology*. Springer. Retrieved from https://ebookcentral.proquest.com/lib/kxp/detail.action?docID=5996299

Lausch, A., Borg, E., Bumberger, J., Dietrich, P., Heurich, M., Huth, A., et al. (2018). Understanding forest health with remote sensing, part III: Requirements for a scalable multi-source forest health monitoring network based on data science approaches. *Remote Sensing*, *10*(7), 1120. https://doi.org/10.3390/rs10071120

Lee, H., Calvin, K., Dasgupta, D., Krinner, G., Mukherji, A., Thorne, P. W., et al. (2023). *IPCC, 2023: Climate change 2023: Synthesis report. Contribution of working groups I, II and III to the sixth assessment report of the intergovernmental panel on climate change*. IPCC. https://doi.org/10.59327/IPCC/AR6-9789291691647

Li, X. [X.], Wigneron, J.-P., Frappart, F., Fan, L., Ciais, P., Fensholt, R., et al. (2021). Global-scale assessment and inter-comparison of recently developed/reprocessed microwave satellite vegetation optical depth products. *Remote Sensing of Environment*, *253*, 112208. https://doi.org/10.1016/j.rse.2020.112208

Ling, Y., Teng, S., Liu, C., Dash, J., Morris, H., & Pastor-Guzman, J. (2022). Assessing the accuracy of Forest phenological extraction from Sentinel-1 C-Band backscatter measurements in deciduous and coniferous forests. *Remote Sensing*, *14*(3), 674. https://doi.org/10.3390/rs14030674

Liu, J. G. (2000). Smoothing Filter-based Intensity Modulation: A spectral preserve image fusion technique for improving spatial details. *International Journal of Remote Sensing*, *21*(18), 3461–3472. https://doi.org/10.1080/014311600750037499

Luo, J., Ying, K., & Bai, J. (2005). Savitzky–golay smoothing and differentiation filter for Even number data. *Signal Processing*, *85*(7), 1429–1434. https://doi.org/10.1016/j.sigpro.2005.02.002

Lyapustin, A., & Wang, Y. (2022). MODIS/terra+Aqua land surface BRF daily L2G global 500m and 1km SIN grid V061 [Dataset]. https://doi.org/10.5067/MODIS/MCD19A1.061

Martínez-Vilalta, J., Anderegg, W. R. L., Sapes, G., & Sala, A. (2019). Greater focus on water pools May improve our ability to understand and anticipate drought-induced mortality in plants. *New Phytologist*, *223*(1), 22–32. https://doi.org/10.1111/nph.15644

Marx, A. (2022). *Dürren in Deutschland* [Helmholtz-Zentrum für Umweltforschung GmbH]. Retrieved from https://www.ufz.de/index.php?de=47252

McDowell, N., Pockman, W. T., Allen, C. D., Breshears, D. D., Cobb, N., Kolb, T., et al. (2008). Mechanisms of plant survival and mortality during drought: Why do some plants survive while others succumb to drought? *New Phytologist*, *178*(4), 719–739. https://doi.org/10.1111/j.1469-8137.2008.02436.x

McDowell, N., Sapes, G., Pivovaroff, A., Adams, H. D., Allen, C. D., Anderegg, W. R. L., et al. (2022). Mechanisms of woody-plant mortality under rising drought, CO_2 and vapour pressure deficit. *Nature Reviews Earth and Environment*, *3*(5), 294–308. https://doi.org/10.1038/s43017-022-00272-1

McKee, T. B., Doesken, N. J., & Kleist, J. (1993). The relationship of drought frequency and duration to time scales. Retrieved from https://climate.colostate.edu/pdfs/relationshipofdroughtfrequency.pdf

Mein, R. G., & Larson, C. L. (1973). Modeling infiltration during a steady rain. *Water Resources Research*, *9*(2), 384–394. https://doi.org/10.1029/WR009i002p00384

Meyer, T., Jagdhuber, T., Piles, M., Fink, A., Grant, J., Vereecken, H., & Jonard, F. (2019). Estimating gravimetric water content of a winter wheat field from L-Band vegetation optical depth. *Remote Sensing*, *11*(20), 2353. https://doi.org/10.3390/rs11202353

Mo, T., Choudhury, B. J., Schmugge, T. J., Wang, J. R., & Jackson, T. J. (1982). A model for microwave emission from vegetation-covered fields. *Journal of Geophysical Research*, *87*(C13), 11229–11237. https://doi.org/10.1029/JC087iC13p11229

Mueller, M. M., Dubois, C., Jagdhuber, T., Hellwig, F. M., Pathe, C., Schmullius, C., & Steele-Dunne, S. (2022). Sentinel-1 backscatter time series for characterization of evapotranspiration dynamics over temperate coniferous forests. *Remote Sensing*, *14*(24), 6384. https://doi.org/10.3390/rs14246384

Myneni, R., Knyazikhin, Y., & Park, T. (2021). MCD15A3H MODIS/terra+Aqua leaf area Index/FPAR 4-day L4 global 500m SIN grid V061 [Dataset]. https://doi.org/10.5067/MODIS/MCD15A3H.061

Nationalpark-Verwaltung. (2023). Nationalpark hainich: Wildnis, buchenurwald, wilde weide, pflanzen, pilze, tiere, geologie und klima, baumkronenpfad. Retrieved from https://www.nationalpark-hainich.de/de/nationalpark/natur.html

Nobel, P. S. (2020). *Physicochemical and environmental plant physiology*. Academic Press. https://doi.org/10.1016/C2018-0-04662-9

Novick, K. A., Ficklin, D. L., Baldocchi, D., Davis, K. J., Ghezzehei, T. A., Konings, A. G., et al. (2022). Confronting the water potential information gap. *Nature Geoscience*, *15*(3), 158–164. https://doi.org/10.1038/s41561-022-00909-2

Okuyama, A., & Imaoka, K. (2015). Intercalibration of advanced microwave scanning radiometer-2 (AMSR2) brightness temperature. In *2015 IEEE international geoscience and remote sensing symposium (IGARSS)*, (pp. 4568–4577). IEEE. https://doi.org/10.1109/tgrs.2015.2402204

Olivares-Cabello, C., Chaparro, D., Vall-llossera, M., Camps, A., & Lopez-Martinez, C. (2023). Global unsupervised assessment of multifrequency vegetation optical depth sensitivity to vegetation cover. *IEEE Journal of Selected Topics in Applied Earth Observations and Remote Sensing*, *16*, 538–552. https://doi.org/10.1109/JSTARS.2022.3226001

O'Neill, P. E., Bindlish, R., Chan, S., Chaubell, M. J., Njoku, E. G., & Jackson, T. (2020a). Soil moisture active passive (SMAP): Algorithm theoretical basis document level 2 and 3 soil moisture (passive) data products. Retrieved from https://nsidc.org/sites/default/files/atbd_spl23_smp_e_revf.pdf

O'Neill, P. E., Chan, S., Njoku, E. G., Jackson, T., Bindlish, R., & Chaubell, M. J. (2020b). SMAP enhanced L3 radiometer global daily 9 km EASE-grid Soil Moisture, version 4 [Dataset]. *NASA National Snow and Ice Data Center Distributed Active*. https://doi.org/10.5067/NJ34TQ2LFE90

Owe, M., Jeu, R. d., & Holmes, T. (2008). Multisensor historical climatology of satellite-derived global land surface moisture. *Journal of Geophysical Research*, *113*(F1), F01002. https://doi.org/10.1029/2007JF000769

Peters, W., Van der Velde, I. R., van Schaik, E., Miller, J. B., Ciais, P., Duarte, H. F., et al. (2018). Increased water-use efficiency and reduced CO_2 uptake by plants during droughts at a continental-scale. *Nature Geoscience*, *11*(9), 744–748. https://doi.org/10.1038/s41561-018-0212-7

Petrolati, D., Gebert, N., Geudtner, D., Bollian, T., Osborne, S., Cesa, M., et al. (2023). An overview of the copernicus Rose-L SAR instrument. In *IGARSS 2023–2023 IEEE international geoscience and remote sensing symposium* (pp. 4310–4313). IEEE. https://doi.org/10.1109/IGARSS52108.2023.10281670

Pfeil, I., Wagner, W., Forkel, M., Dorigo, W., & Vreugdenhil, M. (2020). Does ASCAT observe the spring reactivation in temperate deciduous broadleaf forests? *Remote Sensing of Environment*, *250*, 112042. https://doi.org/10.1016/j.rse.2020.112042

Philipp, M., Wegmann, M., & Kübert-Flock, C. (2021). Quantifying the response of German forests to drought events via satellite imagery. *Remote Sensing*, *13*(9), 1845. https://doi.org/10.3390/rs13091845

Poyatos, R., Granda, V., Flo, V., Adams, M. A., Adorján, B., Aguadé, D., et al. (2021). Global transpiration data from sap flow measurements: The SAPFLUXNET database. *Earth System Science Data*, *13*(6), 2607–2649. https://doi.org/10.5194/essd-13-2607-2021

Proietti, R., Antonucci, S., Monteverdi, M. C., Garfì, V., Marchetti, M., Plutino, M., et al. (2020). Monitoring spring phenology in mediterranean beech populations through in situ observation and synthetic aperture radar methods. *Remote Sensing of Environment*, *248*, 111978. https://doi.org/10.1016/j.rse.2020.111978

Rakovec, O., Samaniego, L., Hari, V., Markonis, Y., Moravec, V., Thober, S., et al. (2022). The 2018–2020 multi-year drought sets a new benchmark in Europe. *Earth's Future*, *10*(3), e2021EF002394. https://doi.org/10.1029/2021EF002394

Rao, K., Anderegg, W. R., Sala, A., Martínez-Vilalta, J., & Konings, A. G. (2019). Satellite-based vegetation optical depth as an indicator of drought-driven tree mortality. *Remote Sensing of Environment*, *227*, 125–136. https://doi.org/10.1016/j.rse.2019.03.026

Rao, K., Williams, A. P., Flefil, J. F., & Konings, A. G. (2020). SAR-Enhanced mapping of live fuel moisture content. *Remote Sensing of Environment*, *245*, 111797. https://doi.org/10.1016/j.rse.2020.111797

Reichardt, K., & Timm, L. C. (2020). *Soil, plant and atmosphere: Concepts, processes and applications*. *Springer eBook Collection*. Springer. https://doi.org/10.1007/978-3-030-19322-5

Riedel, T., Pathe, C., Thiel, C., Herold, M., & Schmullius, C. (2002). Systematic investigation on the effect of dew and interception on multifrequency and multipolarimetric radar backscatter signals. In A. Wilson & S. Quegan (Chairs) (Eds.), *Retrieval of Bio- and geo-physical parameters from SAR data for land applications*.

Rodríguez-Fernández, N. J., Mialon, A., Mermoz, S., Bouvet, A., Richaume, P., Al Bitar, A., et al. (2018). An evaluation of SMOS L-band vegetation optical depth (L-VOD) data sets: High sensitivity of L-VOD to above-ground biomass in Africa. *Biogeosciences*, *15*(14), 4627–4645. https://doi.org/10.5194/bg-15-4627-2018

Rüetschi, M., Small, D., & Waser, L. (2019). Rapid detection of windthrows using Sentinel-1 C-Band SAR data. *Remote Sensing*, *11*(2), 115. https://doi.org/10.3390/rs11020115

Savitzky, A., & Golay, M. J. E. (1964). Smoothing and differentiation of data by simplified least squares procedures. *Analytical Chemistry*, *36*(8), 1627–1639. https://doi.org/10.1021/ac60214a047

Schellenberg, K., Jagdhuber, T., Zehner, M., Hese, S., Urban, M., Urbazaev, M., et al. (2023). Potential of Sentinel-1 SAR to assess damage in drought-affected temperate deciduous broadleaf forests. *Remote Sensing*, *15*(4), 1004. https://doi.org/10.3390/rs15041004

Schuldt, B., Buras, A., Arend, M., Vitasse, Y., Beierkuhnlein, C., Damm, A., et al. (2020). A first assessment of the impact of the extreme 2018 summer drought on Central European forests. *Basic and Applied Ecology*, *45*, 86–103. https://doi.org/10.1016/j.baae.2020.04.003

Soudani, K., Delpierre, N., Berveiller, D., Hmimina, G., Vincent, G., Morfin, A., & Dufrêne, É. (2021). Potential of C-band synthetic aperture radar Sentinel-1 time-series for the monitoring of phenological cycles in a deciduous forest. *International Journal of Applied Earth Observation and Geoinformation*, *104*, 102505. https://doi.org/10.1016/j.jag.2021.102505

Steele-Dunne, S. C., McNairn, H., Monsivais-Huertero, A., Judge, J., Liu, P.-W., & Papathanassiou, K. (2017). Radar remote sensing of agricultural canopies: A review. *IEEE Journal of Selected Topics in Applied Earth Observations and Remote Sensing*, *10*(5), 2249–2273. https://doi.org/10.1109/JSTARS.2016.2639043

Tang, Y., Wang, L., Yu, Y., & Lu, D. (2022). Differential response of plant transpiration to uptake of rainwater-recharged soil water for dominant tree species in the semiarid Loess Plateau. *Hydrology and Earth System Sciences*, *26*(19), 4995–5013. https://doi.org/10.5194/hess-26-4995-2022

Thonfeld, F., Gessner, U., Holzwarth, S., Kriese, J., Da Ponte, E., Huth, J., & Kuenzer, C. (2022). A first assessment of canopy cover loss in Germany's forests after the 2018–2020 drought years. *Remote Sensing*, *14*(3), 562. https://doi.org/10.3390/rs14030562

TMIL. (2022). *Waldzustandsbericht 2022: Forstliches Umweltmonitoring in Thüringen*. Thüringer Ministerium für Infrastruktur (TMIL). Retrieved from https://infrastruktur-landwirtschaft.thueringen.de/fileadmin/Forst_und_Jagd_Fischerei/Forstwirtschaft/2022_Waldzustandsbericht_barrierefrei.pdf

Torres, R., Geudtner, D., Davidson, M., Bibby, D., Traver, I. N., Isabel, A., et al. (2022). Copernicus Sentinel-1 next generation mission: Enhanced C-Band data continuity. In *Igarss 2022–2022 IEEE international geoscience and remote sensing symposium*, (pp. 4717–4719). IEEE. https://doi.org/10.1109/IGARSS46834.2022.9883365

Truckenbrodt, J., Cremer, F., Baris, I., & Eberle, J. (2019a). pyroSAR: A framework for large-scale SAR satellite data processing: Proc. Big Data from Space, (pp. 19–20). https://doi.org/10.13140/RG.2.2.16424.83206

Truckenbrodt, J., Freemantle, T., Williams, C. [C.], Jones, T., Small, D., Dubois, C., et al. (2019b). Towards Sentinel-1 SAR analysis-ready data: A best practices assessment on preparing backscatter data for the cube [Dataset]. *Data*, *4*(3), 93. https://doi.org/10.3390/data4030093

Tucker, C. J., & Sellers, P. J. (1986). Satellite remote sensing of primary production. *International Journal of Remote Sensing*, *7*(11), 1395–1416. https://doi.org/10.1080/01431168608948944

Ulaby, F. T., Moore, R. K., & Fung, A. K. (1986). Microwave remote sensing: Active and passive. In *From theory to applications* (Vol. 3). Artech House. Retrieved from https://www.worldcat.org/isbn/978-0890061923

United States Geological Survey. (2023). Normalized difference moisture index. Retrieved from https://www.usgs.gov/landsat-missions/normalized-difference-moisture-index

Vaca, C. C., & Van der Tol, C. (2018). Sensitivity of Sentinel-1 to rain stored in temperate forest. In *2018 IEEE international geoscience and remote sensing Symposium IGARSS*, (pp. 5330–5333). IEEE. https://doi.org/10.1109/IGARSS.2018.8517859

Vreugdenhil, M., Wagner, W., Bauer-Marschallinger, B., Pfeil, I., Teubner, I., Rüdiger, C., & Strauss, P. (2018). Sensitivity of Sentinel-1 backscatter to vegetation dynamics: An Austrian case Study. *Remote Sensing*, *10*(9), 1396. https://doi.org/10.3390/rs10091396

Wang, C., Fu, B., Zhang, L., & Xu, Z. (2019). Soil moisture–plant interactions: An ecohydrological review. *Journal of Soils and Sediments*, *19*(1), 1–9. https://doi.org/10.1007/s11368-018-2167-0

Wang, H., Wigneron, J.-P., Ciais, P., Yao, Y., Fan, L., Liu, X., et al. (2023). Seasonal variations in vegetation water content retrieved from microwave remote sensing over amazon intact forests. *Remote Sensing of Environment*, *285*, 113409. https://doi.org/10.1016/j.rse.2022.113409

WMO. (2012). *Standardized precipitation index user guide: No. 1090. world Meteorological Organization. WMO* (Vol. 1091). WMO. Retrieved from https://www.worldcat.org/isbn/9789263110916

Yao, Y., Humphrey, V., Konings, A. G., Wang, Y., Yin, Y., Holtzman, N., et al. (2024). Investigating diurnal and seasonal cycles of vegetation optical depth retrieved from GNSS signals in a broadleaf forest. *Geophysical Research Letters*, *51*(6), e2023GL107121. https://doi.org/10.1029/2023GL107121

Zehner, M., Dubois, C., Thiel, C., Schellenberg, K., Rüetschi, M., Brenning, A., et al. (2023). Accounting for deciduous forest structure and viewing geometry effects improves Sentinel-1 time series image consistency. *IEEE Transactions on Geoscience and Remote Sensing*, *61*, 1–13. https://doi.org/10.1109/TGRS.2023.3310113

Zhao, M., Humphrey, V., Feldman, A. F., & Konings, A. G. (2024). Temperature is likely an important omission in interpreting vegetation optical depth. *Geophysical Research Letters*, *51*(15), Article e2024GL110094. https://doi.org/10.1029/2024GL110094